

Searching from Area to Point: A Semantic Guided Framework with Geometric Consistency for Accurate Feature Matching

Yesheng Zhang, Xu Zhao, *Member, IEEE*, Dahong Qian, *Senior Member, IEEE*

Abstract—Feature matching is a crucial technique in computer vision. A unified perspective for this task involves treating it as a search problem, with the objective of developing an efficient search strategy to narrow down the search space to achieve point matches between images. The search space is a key element which affects the search strategy design, but it is often not well defined in current approaches, leading to limited accuracy in matching. This paper, thus, proposes a novel search space for precise feature matching, named semantic area matches, which consists of matched image areas containing prominent semantic. This search space facilitates point matching by reducing the matching difficulty and enables recent detector-free matching methods to handle high-resolution input. For the search strategy corresponding to this search space, we propose a hierarchical feature matching framework called *Area to Point Matching* (A2PM), which involves identifying semantic area matches between images and subsequently performing point matching on these area matches. Additionally, we propose the *Semantic and Geometry Area Matching* (SGAM) method to implement this framework, which leverages semantic priors and geometric consistency to establish precise area and point matches between images. By integrating the SGAM method with off-the-shelf detector-free matchers to adopt the A2PM framework, our proposed method demonstrates significant performance improvement in extensive point matching (up to +29.16%) and pose estimation (up to +11.04%) experiments. The code is publicly available at <https://github.com/Easonyesheng/SGAM>.

Index Terms—Feature matching, pose estimation, Correspondence Estimation, Epipolar Geometry

I. INTRODUCTION

FEATURE matching is a fundamental task in computer vision, which serves as the basis of a wide range of vision applications, such as simultaneous localization and mapping [1], structure from motion [2] and image alignment [3]. Despite its status as a well-studied task, accurately determining the projections of a single 3D point in two different viewpoints continues to pose challenges. These challenges arise from potential extreme viewpoints, light variations, repetitive patterns, and motion blur, all of which contribute to the limited accuracy in the downstream two-view geometry estimation.

In pursuit of high precision feature matching, this paper proposes a unified searching perspective for this task. Given

Yesheng Zhang and Xu Zhao are with the Department of Automation, School of Electronic Information and Electrical Engineering, Shanghai Jiao Tong University, Shanghai 200240, China.(email: preacher@sjtu.edu.cn; zhaoxu@sjtu.edu.cn, *Corresponding author: Xu Zhao*).

Dahong Qian is with The School of Biomedical Engineering, Shanghai Jiao Tong University, Shanghai 200240, China. (email: dahong.qian@sjtu.edu.cn)

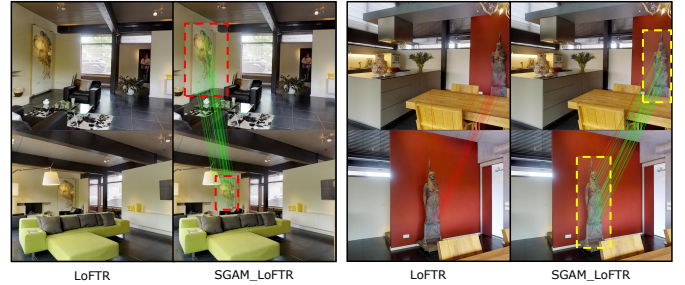


Fig. 1. Performance comparison on MatterPort3D. The dashed boxes are area matches obtained by SGAM, providing current point matchers with reasonable search space (left, where the original LoFTR failed) and high input image resolution (right) to achieve significant performance improvement.

the source point in one image, determining the correspondence in the other image involves searching for the target point from a specific set (the search space) by a carefully designed approach (the search strategy). Therefore, the search space and search strategy are crucial for this searching task. Specifically, the search space is a set containing the targets, which vary through different search phases. It functions as the input or output of the search strategy, which aims to narrow down the input search space to the target one. Hence, a well-defined search space accompanied by an effective search strategy ensure high precision in searching (Fig. 1).

Current feature matching methods are divided into detector-based and detector-free frameworks depending on whether a detector is used. However, taking this unified searching perspective into consideration, the fundamental disparity primarily arises from the distinct search spaces, which leads to the employment of different search strategies. In the detector-based framework [4], [5], the search space is first reduced from the entire image to the keypoint set, from which the correspondences are subsequently established. On the other hand, patch-level correspondences are utilized as the mid-level search space in the detector-free framework [6], [7]. These correspondences are obtained through dense feature comparison between images. Then, point matches are refined from these matched patches.

While finding point matches from keypoint set is easy in the detector-based framework, detecting keypoints even with deep CNN [8], [9] in the image, however, suffers from inaccurate and failed detection caused by rapid change in viewpoint, varied illumination, complex 3D geometry and motion blur. Thus the keypoint set is not a suitable mid-level search space

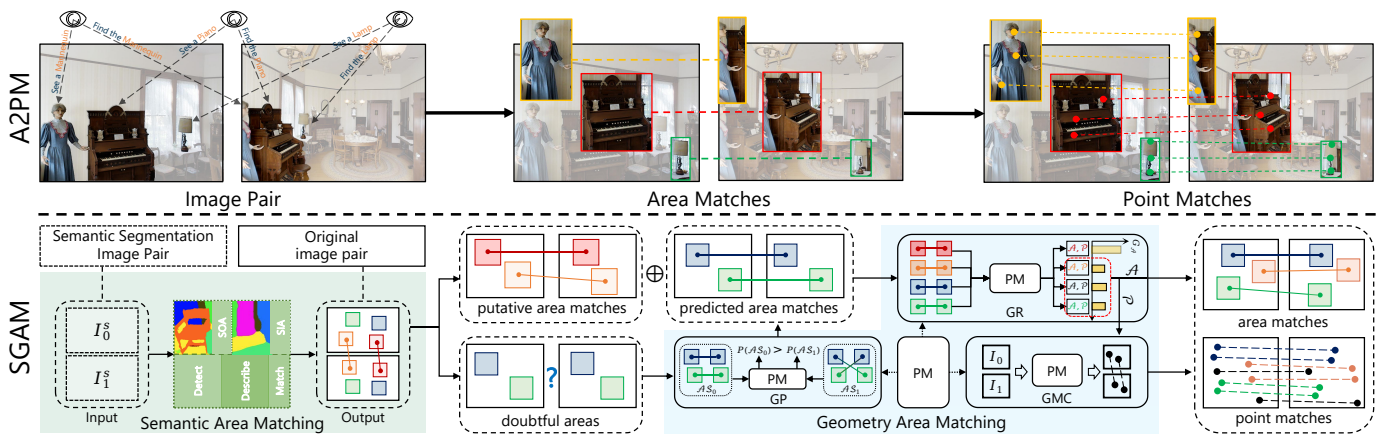


Fig. 2. **Overview of the proposed feature matching method.** (i) **Top:** The proposed *Area to Point Matching* (A2PM) framework initially identifies semantic area matches between images and then conducts point matching within the matched areas. (ii) **Bottom:** We propose *Semantic and Geometry Area Matching* (SGAM) method, which encompasses *Semantic Area Matching* (SAM) and *Geometry Area Matching* (GAM). The SAM leverages semantic segmentation to detect and match *semantic object areas* (SOA) and *semantic intersection areas* (SIA) between the images. Integrated with an off-the-shelf *Point Matcher* (PM), the GAM comprises a *Predictor* (GP) for determining true matches within doubtful areas, a *Rejector* (GR) for filtering out false and poor area matches and a *Global Match Collection* (GMC) module to further enhance the robustness under low semantic scenes, by collecting accurate global correspondences.

as it is difficult to obtain reliably. The detector-free framework [10] adopts the dense search strategy in the entire image and takes patch-level matches as the mid-level search space, where the point-wise match refinement is performed. Attention mechanism is utilized in this effective coarse-to-fine framework to endow perception of global context and achieves SOTA performance [7], [11]–[13]. Nevertheless, the patch matches lack clear definitions related to image contents, resulting in expensive feature computations to obtain them. Therefore, in the coarse level, the full-image feature extraction and attention computation have to be implemented in size-reduced images for acceptable computation cost, in which much detailed information is lost, limiting the matching accuracy. Recently, another two-stage matching method, MKPC [14], achieves the co-visible area between images as the mid-level search spaces by off-the-shelf point matcher, but the individual co-visible area is too rough and its accuracy suffers from stage-one matching. PATS [15] utilizes evenly cropped image patches as the mid-level search space, but achieving these matches necessitates multiple iterations, thereby incurring additional computational costs. In summary, existing feature matching methods suffer from a lack of appropriate search space and corresponding search strategy, limiting the matching precision.

To tackle this problem, we propose to utilize semantic information in images to establish a novel search space for feature matching. Firstly, the study of semantic understanding in images is well-established, and recent semantic segmentation methods [16] demonstrate exceptional accuracy and generalization, naturally generating multiple areas containing substantial semantic information inside the image, termed as *semantic areas*. Due to the invariance of semantic to viewpoint, illumination, and scale [17]–[19], precise semantic segmentation enables seamless matching of *semantic areas* between images. Thus, the *semantic area matches* are easily accessible. On the other hand, the *semantic areas* facilitate inside point match searching, since distinct image features that aid in accurate point matching are typically concentrated within these areas. Meanwhile, the area-based computation is

more feasible compared to entire-image-based computation. Hence, utilizing this *semantic area matches* as the initial search space for detector-free methods leads to more reliable point matching and allows for high-resolution inputs, ultimately improving the matching performance. Therefore, the *semantic area matches* are proper to serve as both the mid-level search space for feature matching and the primary search space for off-the-shelf detector-free methods.

In order to align the proposed search space with an efficient search strategy, we propose a hierarchical feature matching framework: *Area to Point Matching* (A2PM, Fig.2 top). This framework contains two search phases: matching semantic areas from the entire images and matching points from the matched areas. For the first phase, we introduce *Semantic Area Matching* (SAM), utilizing the semantic prior to efficiently detect and match semantic areas between images. In specific, SAM leverages semantic segmentation images as input to match two types of image areas: semantic object areas and semantic intersection areas. Through a process of detection, description, and matching, putative area matches are achieved. However, the use of semantic abstraction in SAM, which omits local details, can introduce *semantic ambiguity* during matching, particularly when distinct instances coexist within the image. Therefore, SAM also identifies doubtful areas that cannot be confidently matched.

Besides doubtful areas, the scene-dependent semantic ambiguity may also lead to erroneous area matches in SAM, negatively impacting feature matching. Therefore, we turn to the inherent geometry property of area matches. Specifically, considering that area matches in images signifies the same 3D entity, the constraint of epipolar geometry naturally applies, regardless of the scene. Furthermore, area matches in the same image pair must adhere to the same constraint, named geometric consistency, which can be employed to address the semantic ambiguity. Thus, we establish the geometric consistency of area matches by utilizing fundamental matrices of point matches within these areas. It enables the proposed *Geometry Area Matching* (GAM) to integrate an

off-the-shelf point matcher for accurate determination of area matches. In practice, the GAM first predicts true area matches from doubtful candidates generated by SAM (GAM Predictor, GP). Subsequently, all area matches undergo filtering by the GAM Rejector (GR) to identify matches with superior geometric consistency. The point matches within accurate area matches are obtained concurrently, thereby completing the second search phase of the A2PM. Furthermore, to handle the correspondence aggregation issue in less-semantic scenes, the Global Match Collection module (GMC) is incorporated in GAM, which involves collecting additional point matches globally based on the geometry consistency of inside-area matches. The GMC ensures the generation of well-distributed matches, advantageous for downstream tasks. Through the combination of SAM and GAM, our *Semantic and Geometry Area Matching* (SGAM, Fig. 2 bottom) is capable of achieving accurate area and point matching between images.

In sum, this work presents the following contributions:

- 1) A well-defined search space for feature matching, i.e. the semantic area matches, is proposed under a hierarchical feature matching framework: A2PM, which narrows down the matching search space to area matches with prominent semantic for precise point matching.
- 2) To implement the A2PM framework, we propose the SGAM approach, which consists of two components: SAM, responsible for identifying putative area matches according to semantics, and GAM, which obtains precise area and point matches by ensuring geometry consistency.
- 3) Our method provides detector-free methods with a suitable search space and high-resolution input (Fig. 1), thereby achieving notable improvements in matching precision (up to +29.16%) and pose estimation performance (up to +11.04%), with semantic segmentation achieved by SEEM as the input.

II. RELATED WORK

A. Detector-based Matching

Detector-based matching relies on detected keypoints and their descriptors [4], [20]. Through the nearest neighbor search based on descriptor distances, point matches can be established between images. In the age of deep learning, recent work [5], [9], [21], [22] utilize deep CNN to achieve better learning feature. Specifically, SuperPoint [5] is early in providing feature detection and description networks and outperforms conventional methods. Subsequent work [8], [9], [23] leverage a unified network to detect and describe feature. At the same time, detached learning detection [24]–[26] and description [27]–[29] are proposed as well. After feature detection, point match searching and outlier rejection are also advanced by recent learning methods [30]–[35]. Essentially, this framework relies on extremely fine-grained search space establishment, i.e. the feature points, to achieve accurate point matching. However, feature point detection poses significant challenges in scenes with low texture, repetitive patterns, extreme changes in illumination and scale, which ultimately leads to a decline in performance. In contrast, our A2PM framework appropriately

TABLE I
SYMBOL TABLE. THE TABLE PROVIDES A COMPREHENSIVE LIST OF SYMBOLS USED IN THE PAPER, AND BRIEF DESCRIPTIONS FOR EACH.

Symbol	Description
I_i	Input image pair, $i \in \{0, 1\}$
I_i^s	Semantic segmentation of I_i , $i \in \{0, 1\}$.
\mathcal{M}_A	A2PM framework.
AM	Area Matching method.
PM	Point Matching method.
α_i	An area in I_0 with i as the index.
β_i	An area in I_1 with i as the index.
$\pi(i)$	Index mapping between matched areas.
$\pi_l(i)$	$\pi(i)$ with index l , indicating the l -th area matching possibility.
$\mathcal{A}_{i,\pi(i)}$	$\mathcal{A}_{i,\pi(i)} = (\alpha_i, \beta_{\pi(i)})$, a matched area pair.
(p, q)	A matched point pair, $q \in I_0, p \in I_1$.
\mathcal{P}_i	A set of M point matches, i is the index of point match set, m is the index of point pair inside the set.
F_i	Fundamental matrix with index i .
$d_{i,j} = D(F_i, \mathcal{P}_j)$	Sampson distance calculated by F_i and \mathcal{P}_j .
$d_{i,i}^m$	Single match Sampson distance, calculated by F_i and a point pair (q_i^m, p_i^m) .
$G_{\mathcal{A}_{i,\pi(i)}}$	Geometry consistency of $\mathcal{A}_{i,\pi(i)}$.
SAM	Semantic Area Matching module.
SOA	Semantic Object Area.
$\mathcal{A}_{i,\pi(i)}^O$	$\mathcal{A}_{i,\pi(i)}^O = (\alpha_i^O, \beta_{\pi(i)}^O)$, a SOA match.
$H_{i,\pi(i)}$	Hamming distance between descriptors of $\mathcal{A}_{i,\pi(i)}^O$.
T_H	Threshold for $H_{i,\pi(i)}$ in SOA matching.
T_{da}	Threshold for the doubtful area.
SIA	Semantic Intersection Area.
$\mathcal{A}_{i,\pi(i)}^I$	$\mathcal{A}_{i,\pi(i)}^I = (\alpha_i^I, \beta_{\pi(i)}^I)$, a SIA match.
$L_{i,\pi(i)}$	l_2 distance between descriptors of $\mathcal{A}_{i,\pi(i)}^I$.
T_L	Threshold for $L_{i,\pi(i)}$ in SIA matching.
GP_{PM}	Geometric area match Predictor, combined with point matcher PM .
GR_{PM}	Geometric area match Rejector, combined with point matcher PM .
GMC_{PM}	Global Match Collection module with PM .
T_{GR}	Threshold of geometry consistency in GR .
\mathcal{AS}_l	$\mathcal{AS}_l = \{\mathcal{A}_{i,\pi_l(i)}\}_i^R$, a set of R area matches with index l related to $\pi_l(i)$.
$G_{\mathcal{AS}_l}$	Geometry consistency of area match set \mathcal{AS}_l .
$SP_{\{\mathcal{A}_{i,\pi(i)}\}_i^T}$	Size Proportion of area matches $\{\mathcal{A}_{i,\pi(i)}\}_i^T$ in the image pair.
T_{SP}	Threshold of size proportion in GMC .

reduces the search space to semantic area matches, which are more robust due to their semantic invariance.

B. Detector-free Matching

In order to avoid detection failure, detector-free framework is proposed [10], [36], [37], aiming at jointly trainable feature detection, matching and outlier rejection to establish point matches directly from image pairs. Initially, 4D CNN is used to extract dense image features [36], [38], [39]. Recent DKM [40] constructs a Gaussian Process using CNN and achieves leading performance. Meanwhile, owing to limited receptive field [10] of CNN, some methods [10], [37] incorporate Transformer [41] to process dense feature extracted by CNN, attaining

SOTA performance. However, the global search space in this framework leads to redundant computation, limiting the resolution of input images. Furthermore, the redundant search space introduces noise from non-overlapping areas in the image pair, resulting in degraded precision of attention operations. As a solution, we propose the A2PM framework, which performs area matching in images prior to point matching. Due to the higher resolution and less noise in area matches, subsequent inside-area point matching precision is improved.

C. Coarse-to-Fine Matching

To avoid high computation costs due to the redundant full-image search space in detector-free matching, coarse-to-fine methods are proposed. In LoFTR [10], patch-level correspondences are established through feature attention of the coarse level matching, which serves as the initial search space for the fine level matching. This approach significantly reduces time consumption compared to the vanilla Transformer [37]. Subsequent works [7], [11]–[13] have improved the attention mechanism to construct a more efficient and precise coarse search space. However, this patch-level search space lacks a clear association with image apparent features or high-level semantics, thus requiring expensive feature comparison for correspondence establishment. The accuracy issue in the coarse level also persists due to low input resolution. PATS [15] is proposed to extract more accurate features from equally cropped image patches with high resolution, but finding patch matches requires multiple iterations. Recent MKPC [14] provides another two-stage feature matching strategy, which utilizes stage-one point matching on the entire images to achieve the co-visible area. Then the stage-two point matching is performed inside it. However, individual co-visible area matching is too rough for precise point matching and its accuracy is entangled with the stage-one point matching. In contrast, our method offers a well-defined search space, i.e. the semantic area matches, along with an independent area matching method utilizing both semantic and geometry priors. It is able to provide a fine-grained search space for detector-free matchers, improving their matching performance.

III. FORMULATION

In this section, we define the proposed A2PM framework and establish a foundation of geometry consistency for our method. Symbols used in this section can be found in Tab. I.

A. Framework Formulation

Generally, given an image pair (I_0, I_1) , an Area Matching method AM and a detector-free Point Matching method PM , our A2PM framework (\mathcal{M}_A) is formulated as:

$$\mathcal{P} = \mathcal{M}_A(I_0, I_1, AM, PM) \quad (1)$$

The output $\mathcal{P} = \{q^m, p^m\}_m^M$ is the set of point matches.

Specifically, we formulate the first search phase from the image pair to area matches as follows. Suppose areas in I_0, I_1 are respectively $\{\alpha_i\}_i$ and $\{\beta_j\}_j$. The area match is

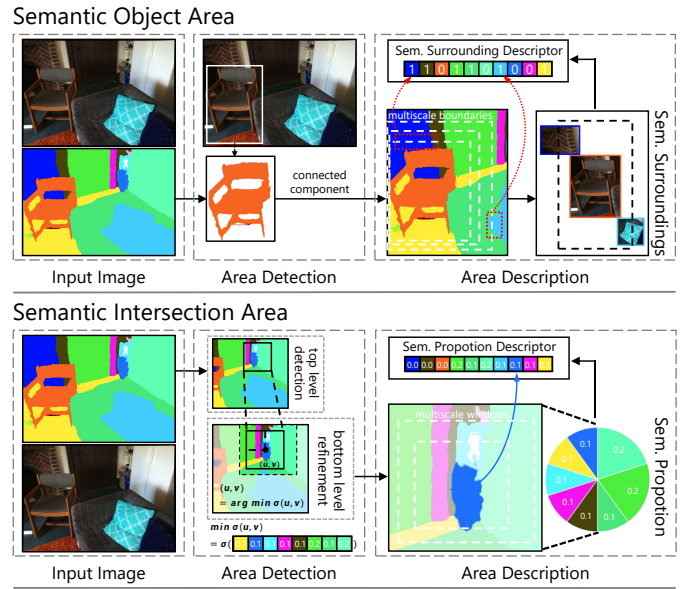


Fig. 3. **Semantic Area Matching (SAM)**. SAM divides image areas into two types to process. For both types of areas, area detection and description are performed first, and then area matching is based on specially-designed descriptor distance minimization.

represented as $\mathcal{A}_{i,j} = (\alpha_i, \beta_j)$. Therefore, N pairs of area matches can be achieved by our AM :

$$\{\mathcal{A}_{i,\pi(i)}\}_i^N = AM(I_0, I_1) \quad (2)$$

where $\pi(i) : \mathbb{R} \rightarrow \mathbb{R}$ is the index mapping between matched areas. Then, point matches inside area matches can be found:

$$\mathcal{P} = PM(\{\mathcal{A}_{i,\pi(i)}\}_i^N) \quad (3)$$

Due to the proper search space of semantic area matches, the matching accuracy of PM is improved. Moreover, the area matches possess higher resolution than the original input of PM , leading to more precise matches.

B. Geometry Consistency Formulation

In order to leverage the inherent geometry property of area matching to improve matching accuracy and robustness, we proceed to formulate the geometry consistency of area matching. Since the geometry constraint of point matches is formed completely, we utilize the point matches within areas and their fundamental matrices to construct the geometry consistency of area matches. First, the correspondences $\mathcal{P}_i = \{(q_i^m, p_i^m)\}_m^M$ in $\mathcal{A}_{i,\pi(i)}$ can be achieved by PM and the fundamental matrix F_i can be calculated as well. Then we form the geometry consistency between \mathcal{P}_i and F_i by Sampson distance [42]:

$$\begin{aligned} d_{i,i} &= \sum_m^M \frac{(p_i^{mT} F_i q_i^m)^2}{(F_i q_i^m)_1^2 + (F_i q_i^m)_2^2 + (F_i^T p_i^m)_1^2 + (F_i^T p_i^m)_2^2} \\ &= \sum_m^M \hat{d}_{i,i}^m = D(F_i, \mathcal{P}_i) \end{aligned} \quad (4)$$

where $(F_i q_i^m)_k$ represents the k -th entry of the vector $F_i q_i^m$. It should be ideally closed to 0 and reflects the matching

precision of $\mathcal{A}_{i,\pi(i)}$, as only the correct area match will produce accurate point matches. Similarly, we can deduce the geometry consistency across area matches. Given two correct area matches $\{\mathcal{A}_{i,\pi(i)}, \mathcal{A}_{j,\pi(j)}\}$ between the images, they should generate the same Fundamental matrix. Thus the cross Sampson distance ($d_{i,j}$) should be close to 0:

$$d_{i,j} = D(F_i, \mathcal{P}_j) \rightarrow 0 \quad (5)$$

Therefore, in an area match set $\{\mathcal{A}_{i,\pi(i)}\}_i^N$, assuming most of area matches are correct, the geometry consistency of a specific area match $\mathcal{A}_{i,\pi(i)}$ can be formulated as:

$$G_{\mathcal{A}_{i,\pi(i)}} = \frac{1}{N} \sum_j^N d_{i,j} \quad (6)$$

Thus, the $G_{\mathcal{A}_{i,\pi(i)}}$ can reflect the matching accuracy of $\mathcal{A}_{i,\pi(i)}$ and the smaller the higher area matching precision.

IV. METHODOLOGY

In this section, we propose the *Semantic and Geometry Area Matching* method that leverages semantic and geometry priors to construct an efficient feature matching search space, rather than relying on additional point matching [14]. Firstly, we introduce the *Semantic Area Matching* (Sec. IV-A) to find putative area matches, leveraging semantic prior. Secondly, we describe the *Geometry Area Matching* (Sec. IV-B), which utilizes geometry consistency to increase the accuracy and robustness of area matching. Finally, the implementation of A2PM framework by combining SGAM with an off-the-shelf detector-free point matcher is illustrated (Sec. IV-C). Symbols in this section are summarised in Tab. I.

A. Semantic Area Matching

To establish semantic area matches between images, we propose a detector-based method, including semantic area detection and description, in light of detector-based point matching. Therefore, we first carefully define the semantic area with the goal of enabling it to serve as an efficient search space for feature matching. A typical semantic area is an object-centred area, termed as *Semantic Object Area* (SOA), whose textured surface or prominent edges favours feature matching. However, some objects (e.g. objects very close to the camera) are so large in the image that the sizes or aspect ratios of the corresponding areas are extremely large, leading to improper search space. Thus, we further propose the *Semantic Intersection Area* (SIA), which consists of intersecting parts of multiple objects rather than an entire object, to efficiently grab solid features of above large objects for feature matching. Afterwards, we illustrate the matching processes of SOA and SIA (Fig. 3) respectively.

1) *Semantic Object Area Matching*: Detecting semantic object areas can be accomplished by identifying the connected components with the object semantic in I_i^s and establishing their bounding boxes as the boundaries for the areas. For achieving a sparse extraction, we further merge the spatially proximate areas that exhibit the same semantic.

Algorithm 1: Geometric Area Match Rejector

Input: $\mathcal{AS} = \{\mathcal{A}_{i,\pi(i)}\}_i^S$
Output: $\{\mathcal{A}_{i^*,\pi(i^*)}, \mathcal{P}_{i^*}\}_{i^*}^T, i^* \in [0, S), T \leq S$

- 1 **for** $\mathcal{A}_{i,\pi(i)}$ **in** \mathcal{AS} **do**
- 2 match inside the area match: $\mathcal{P}_i = PM(\mathcal{A}_{i,\pi(i)});$
- 3 calculate the fundamental matrix: $F_i;$
- 4 get the self-geometry consistency by Eq. 4: $d_{i,i};$
- 5 calculate the geometry consistency threshold:
 $T_{GR} = \phi \times \frac{1}{S} \sum_i^S d_{i,i};$
- 6 **for** $\mathcal{A}_{i,\pi(i)}$ **in** \mathcal{AS} **do**
- 7 calculate the $G_{\mathcal{A}_{i,\pi(i)}}$ by Eq. 6;
- 8 **if** $G_{\mathcal{A}_{i,\pi(i)}} > T_{GR}$ **then** reject $\mathcal{A}_{i,\pi(i)};$
- 9 **Output** the left area matches and their correspondences:
 $\{\mathcal{A}_{i^*,\pi(i^*)}, \mathcal{P}_{i^*}\}_{i^*}^T, i^* \in [0, S), T \leq S;$

As SOA already contains the object semantic information, its descriptor is intended to distinguish it from other instances of the same semantics in the image. Since close instances are merged by SOA detection, it is crucial to focus on distinguishing the spatially scattered instances, which are likely to have different surroundings. Therefore, we propose the *semantic surrounding descriptor* to differentiate instances by leveraging semantic information about their surroundings. Initially, four descriptors are constructed as binary zero vectors for each side of SOA. Each bit in these vectors corresponds to a semantic present in the image pair. Subsequently, we record all the semantics that are encountered along the area sides to set the corresponding bits in the binary vectors to true. To enhance scale robustness, we propose the multiscale boundaries capture. By scaling the area boundary to varying degrees, more semantics can be captured by multiscale boundary sides. Finally, the four side vectors are integrated in a specific order to form the SOA descriptor.

The described SOAs are first matched directly by their object semantics, termed as $\{\mathcal{A}_{i,\pi(i)}^O\}_i$. Subsequently, Hamming distances between the binary descriptors ($\{H_{i,\pi(i)}\}_i$) of initial matches are calculated. Next, matches among areas sharing the same semantic are identified through nearest neighbor search. During this process, if the confidences of two candidate matches for α_i , termed as $\mathcal{A}_{i,j}, \mathcal{A}_{i,k}$, subject to $|H_{i,j} - H_{i,k}| < T_{da}$, these areas ($\alpha_i, \beta_j, \beta_k$) are flagged as doubtful. Finally, the matches with $H_{i,\pi(i)} > T_H$ are rejected.

2) *Semantic Intersection Area Matching*: The detection of SIA involves sliding a window across the I_i^s to identify areas with abundant semantics. Specifically, the window size is set to the desired area size, and the slide step is half the window size. During the window sliding, areas with more than 3 different semantics are collected as SIAs. Considering the expensive time cost of window sliding in original I_i^s , we employ a two-layer semantic pyramid. The top layer involves reducing the I_i^s and window to scale r , performing initial detection. The bottom layer is the original I_i^s , used to further refine the area location. In the refinement, we first calculate the proportion of semantics within each area. To ensure that prominent features remain close to the center of the area, we

adjust the area center $((u, v))$ within the range of area size by minimizing the variance of semantic proportion $(\sigma(u, v))$ within it.

To match SIAs across images, the inside-area semantics is crucial. Therefore, we propose using the semantic proportion, calculated during the detection process, as the SIA descriptor. This descriptor takes the form of a vector, with its length corresponding to the number of semantics present in the image pair. Each element within the vector represents a specific semantic, with its value indicating the proportion of that semantic within the area. To enhance the scale robustness, the descriptors are constructed on multiscale windows and then merged by taking their average. The spatial specificity of the descriptor is improved by partitioning the original area into quarters and constructing descriptors for each sub-area. These sub-area descriptors are then combined to form the final one in a specific order.

Afterwards, SIA matches $(\mathcal{A}_{i,\pi(i)}^I)$ can be found by nearest neighbour search based on l_2 distance between descriptors $(\mathcal{L}_{i,\pi(i)})$. Similar to SOA matching, doubtful areas are identified, when $|\mathcal{L}_{i,\pi(i)} - \mathcal{L}_{j,\pi(j)}| < T_{da}$ for area matches $\mathcal{A}_{i,\pi(i)}^I, \mathcal{A}_{j,\pi(j)}^I$. Finally, matches with $\mathcal{L}_{i,\pi(i)} > T_L$ are rejected.

B. Geometry Area Matching

Although the SAM is effective in most cases, it tends to overlook local details in images, which can result in *semantic ambiguity* when multiple instances are present in the image pair. Especially when their semantic surroundings are similar, SAM may obtain doubtful areas and incorrect area matches. Fortunately, area matches, similar to point matches, are inherently constrained by epipolar geometry, which can be utilized to resolve semantic ambiguity. Hence, based on the formulated geometry consistency in Sec. III, we propose *Geometry Area Matching* (GAM) to refine the results of SAM and fulfill the A2PM framework. GAM incorporates a Predictor (GP, Sec. IV-B1) to identify true matches in doubtful areas, a Rejector (GR, Sec. IV-B2) to eliminate false and inferior area matches and a Global Match Collection module (GMC, Sec. IV-B3) to achieve uniformly distributed point matches.

1) *Geometry Area Match Predictor*: The GP aims to determine the true matches among multiple matching possibilities of doubtful areas. Given doubtful areas $\{\alpha_i\}_i^H, \{\beta_i\}_i^R, R \leq H$ in images I_0, I_1 which can not be well matched by SAM, and assume R true area matches exist:

$$\mathcal{AS}_l = \{\mathcal{A}_{i,\pi_l(i)}\}_i^R = \{(\alpha_i, \beta_{\pi_l(i)})\}_i^R \quad (7)$$

where \mathcal{AS}_l is a set of area matches, $\pi_l(i) \in [0, R)$ is an index mapping between matched areas with l indicating different area matching possibilities. There are totally $L = \frac{H!}{(H-R)!}$ matching possibilities ($l \in [0, L)$), and only one true area match set (\mathcal{AS}_{l^*}) exists with the best geometry consistency, as every area match in \mathcal{AS}_{l^*} is correctly matched. Thus, we can form the geometry consistency of every \mathcal{AS}_l based on Eq. 6:

$$G_{\mathcal{AS}_l} = \frac{1}{R} \sum_i^R G_{\mathcal{A}_{i,\pi_l(i)}} \quad (8)$$

Algorithm 2: Global Match Collection

Input: $\{\mathcal{P}_i, \mathcal{A}_{i,\pi(i)}\}_i^T, I_0, I_1, T_{SP}$

Output: \mathcal{P}_g

- 1 calculate the Size Proportion of area matches in images: $SP_{\{\mathcal{A}_{i,\pi(i)}\}_i^T}$
 - 2 **if** $SP_{\{\mathcal{A}_{i,\pi(i)}\}_i^T} < T_{SP}$ **then**
 - 3 initialize the empty collected match list: $\mathcal{P}_g = \emptyset$;
 - 4 calculate the fundamental matrix F_a and mean Sampson distance $\frac{1}{T} \sum_i^T d_{a,i}$ of *inside-area* point matches $\{\mathcal{P}_i\}_i^T$;
 - 5 achieve the global matches: $\mathcal{P}_g = PM(I_0, I_1)$;
 - 6 **for** (p_g^m, q_g^m) **in** \mathcal{P}_g **do**
 - 7 get the single match Sampson distance $\hat{d}_{a,g}^m$;
 - 8 **if** $\hat{d}_{a,g}^m \leq \frac{1}{T} \sum_i^T d_{a,i}$ **then** collect the match (p_g^m, q_g^m) into \mathcal{P}_g ;
 - 9 Output the collected global matches: \mathcal{P}_g ;
-

which can be further written in probabilistic form:

$$P(\mathcal{AS}_l) = \exp(-G_{\mathcal{AS}_l}) \quad (9)$$

Therefore, the \mathcal{AS}_{l^*} can be achieved by geometry consistency maximization:

$$\mathcal{AS}_{l^*} = \operatorname{argmax}_l P(\mathcal{AS}_l) \quad (10)$$

This can be solved by considering the whole density of \mathcal{AS}_l and choose the one with the maximum $P(\mathcal{AS}_l)$.

2) *Geometry Area Match Rejector*: Following the prediction, the GR leverages geometry consistency to identify and disregard potential false matches, thereby enhancing the accuracy of the area matching. Given an area match set $\mathcal{AS} = \{\mathcal{A}_{i,\pi(i)}\}_i^S$ achieved by SAM and GP, the geometry consistency of each $\mathcal{A}_{i,\pi(i)}$ can be measured by $G_{\mathcal{A}_{i,\pi(i)}}$ (Eq. 6). Then, matches with $G_{\mathcal{A}_{i,\pi(i)}}$ exceeding a specific threshold can be discarded as false or inaccurate. In practice, the threshold T_{GR} is based on the mean self-geometry consistency (Eq. 4) with a weight ϕ . The Transformer-based matcher [10], [37] is embedded in GR to acquire precise point matches. The specific process is illustrated in Algorithm 1.

3) *Global Match Collection*: The precision of point matches within area matches is remarkable, termed as $\{\mathcal{P}_i, \mathcal{A}_{i,\pi(i)}\}_i^T$, as a result of the well-defined search spaces achieved through both semantic prior and geometric consistency. However, the distribution of these matches depends on the specific scenes. If less semantic information is available in the scene, there will be a small number of area matches. Consequently, the point matches will cluster, which has a negative impact on the downstream tasks [42]. To enhance the robustness against scenes with limited semantic information, we propose the GMC module to collect global matches (\mathcal{P}_g) utilizing the geometry constraint of accurate inside area matches, when few area matches exist (determined by size proportion threshold T_{SP} , which represents the proportion threshold of the image occupied by matched areas in the image pair). The detailed algorithm is presented in Algorithm 2.

TABLE II

VALUE RESULTS (%) OF MMA. WE REPORT MMA WITH THREE THRESHOLDS UNDER VARIOUS MATCHING DIFFICULTIES. **OUR SGAM** IS APPLIED ON FOUR BASELINES. TO SHOW THE IMPACT OF SEMANTIC ACCURACY TO OUR METHOD, WE TAKE THREE DIFFERENT SEMANTIC INPUTS: **SGAM USING GROUND TRUTH (GT)**, **SGAM USING SEEM-L** AND **SGAM USING SEEM-T**. THE IMPROVEMENT ACHIEVED BY SGAM IS ALSO REPORTED IN PERCENTAGE, WHICH IS IMPRESSIVE TO SHOW THE EFFECTIVENESS OF OUR METHOD.

MMA	ScanNet: FD@5			ScanNet: FD@10			MatterPort3D		
	MMA@1↑	MMA@2↑	MMA@3↑	MMA@1↑	MMA@2↑	MMA@3↑	MMA@1↑	MMA@2↑	MMA@3↑
SP [5]+NN	26.56	59.87	75.75	13.76	40.47	59.49	3.46	17.41	32.43
SP [5]+SG [30]	37.54	63.06	76.15	24.40	43.32	57.57	13.77	21.66	29.95
ASLFeat [9]+NN	28.90	58.69	75.52	15.66	40.98	60.41	6.31	20.59	35.79
ALike [8]+NN	31.99	60.98	75.03	16.41	40.98	59.49	7.25	20.94	34.55
ASpan [7]	32.99	66.91	85.03	25.35	49.83	70.79	7.17	21.10	37.25
GT+SGAM_ASpan	37.88 _{+14.82%}	72.81 _{+8.83%}	89.40 _{+5.14%}	28.19 _{+11.19%}	54.67 _{+9.72%}	75.42 _{+6.53%}	7.68 _{+7.03%}	24.51 _{+16.20%}	39.94 _{+7.21%}
SEEM-L [16]+SGAM_ASpan	36.48 _{+10.58%}	70.70 _{+5.66%}	87.58 _{+2.99%}	27.15 _{+7.09%}	52.85 _{+6.07%}	73.76 _{+4.19%}	7.61 _{+6.11%}	23.98 _{+13.66%}	39.16 _{+5.12%}
SEEM-T [16]+SGAM_ASpan	35.54 _{+7.73%}	69.44 _{+3.79%}	86.64 _{+1.89%}	26.81 _{+5.78%}	52.11 _{+4.59%}	72.84 _{+2.89%}	7.40 _{+3.17%}	22.51 _{+6.69%}	38.41 _{+3.11%}
QuadT [11]	32.79	70.40	88.31	22.67	56.92	78.46	7.44	23.97	41.72
GT+SGAM_QuadT	39.43 _{+20.25%}	75.96 _{+7.89%}	90.94 _{+2.47%}	26.68 _{+17.65%}	62.49 _{+9.79%}	82.32 _{+4.93%}	8.26 _{+11.10%}	26.19 _{+9.29%}	45.56 _{+9.20%}
SEEM-L [16]+SGAM_QuadT	37.02 _{+12.91%}	73.63 _{+4.59%}	89.30 _{+1.12%}	25.17 _{+11.03%}	60.55 _{+6.38%}	81.08 _{+3.35%}	7.91 _{+6.41%}	25.95 _{+8.26%}	43.05 _{+3.17%}
SEEM-T [16]+SGAM_QuadT	36.35 _{+10.85%}	72.54 _{+3.04%}	88.40 _{+0.10%}	24.30 _{+7.15%}	59.38 _{+4.32%}	80.46 _{+2.55%}	7.86 _{+5.63%}	24.50 _{+2.23%}	42.88 _{+2.76%}
LoFTR [10]	30.49	65.33	83.51	17.85	46.78	67.90	9.50	22.08	36.07
GT+SGAM_LoFTR	35.02 _{+14.85%}	70.38 _{+7.73%}	88.06 _{+5.45%}	19.02 _{+6.55%}	49.10 _{+4.95%}	70.55 _{+3.91%}	12.48 _{+31.36%}	29.08 _{+31.74%}	48.31 _{+33.93%}
SEEM-L [16]+SGAM_LoFTR	33.83 _{+10.95%}	70.05 _{+7.23%}	87.33 _{+4.58%}	18.85 _{+5.60%}	48.78 _{+4.27%}	68.90 _{+1.47%}	12.27 _{+29.16%}	27.20 _{+23.22%}	40.25 _{+11.57%}
SEEM-T [16]+SGAM_LoFTR	33.17 _{+10.55%}	69.52 _{+6.40%}	86.71 _{+3.84%}	18.21 _{+2.03%}	47.45 _{+1.42%}	67.98 _{+0.12%}	11.47 _{+20.77%}	25.10 _{+13.69%}	38.45 _{+6.59%}
COTR [37]	32.92	63.45	78.71	16.51	42.36	60.99	10.63	29.37	46.07
GT+SGAM_COTR	36.76 _{+11.67%}	66.56 _{+4.91%}	81.19 _{+3.16%}	18.56 _{+12.42%}	45.45 _{+7.28%}	64.52 _{+5.79%}	12.36 _{+16.36%}	32.64 _{+11.16%}	49.82 _{+8.15%}
SEEM-L [16]+SGAM_COTR	36.54 _{+11.00%}	66.48 _{+4.78%}	81.04 _{+2.96%}	18.16 _{+10.01%}	44.54 _{+5.15%}	63.29 _{+3.76%}	11.73 _{+10.40%}	31.97 _{+8.88%}	48.70 _{+5.71%}
SEEM-T [16]+SGAM_COTR	36.05 _{+9.52%}	65.89 _{+3.85%}	80.48 _{+2.24%}	17.60 _{+6.60%}	43.71 _{+3.18%}	62.50 _{+2.47%}	11.11 _{+4.57%}	31.30 _{+6.58%}	47.49 _{+3.08%}

C. Framework Implementation

In summary, the A2PM framework follows the steps outlined below. First, the framework obtains the putative area matches ($\{A_{i,\pi(i)}^*\}_i^K$) and the doubtful areas ($\{\alpha_i\}_i^H, \{\beta_i\}_i^R$, where $R \leq H$) between the images through semantic segmentation (I_0^s, I_1^s) using the SAM algorithm:

$$\{A_{i,\pi(i)}^*\}_i^K, \{\alpha_i\}_i^H, \{\beta_i\}_i^R = SAM(I_0^s, I_1^s) \quad (11)$$

Next, the doubtful areas are cropped from original images (I_0, I_1) and matched by an off-the-shelf detector-free Point Matcher (PM) integrated in GP to achieve inside-area correspondences for geometry consistency calculation. Then, the R true area matches can be identified by GP_{PM} :

$$\{A_{i,\pi(i)}^*\}_i^R = GP_{PM}(\{\alpha_i\}_i^H, \{\beta_i\}_i^R, I_0, I_1) \quad (12)$$

Afterwards, the accurate area and point matches inside them are achieved by GR integrated with PM ($T \leq K + R$):

$$\{A_{i,\pi(i)}, \mathcal{P}_i\}_i^T = GR_{PM}(\{A_{i,\pi(i)}^*\}_i^{K+R}, I_0, I_1) \quad (13)$$

In case of less-semantic scenes, more accurate point matches from full-image point matching using PM are obtained by our GMC_{PM} module:

$$\mathcal{P}_g^C = GMC_{PM}(\{A_{i,\pi(i)}, \mathcal{P}_i\}_i^T, I_0, I_1, T_{SP}) \quad (14)$$

Finally, the point matches including inside-area matches $\{\mathcal{P}_i\}_i^T$ and global matches \mathcal{P}_g^C are achieved as the output of our SGAM method, which possess both high matching accuracy and uniform spatial distribution. It is noteworthy the PM we utilized can be any detector-free method without re-training or fine-tuning. Therefore, our SGAM is a plug-and-play framework to improve the feature matching precision.

V. RESULTS

A. Dataset

To demonstrate the superiority of the A2PM framework and SGAM method, we evaluate our methods on two different indoor datasets, ScanNet [43] and MatterPort3D [44]. Additionally, we investigated the robustness of our method in diverse semantic scenes by conducting experiments on the outdoor KITTI360 dataset [45] and YFCC100M [46] dataset. First three datasets all offer ground truth semantic labels, which can be directly used as the input of our method. Moreover, we also evaluated the robustness of our method against semantic prior precision by utilizing recent semantic segmentation method, SEEM [16], to perform semantic segmentation. The ScanNet contains numerous sequence images, and we selected image pairs with varying levels of difficulty based on the frame difference from its *scene_0000* to *scene_0299* to evaluate our method. We also compare with other SOTA methods on the standard ScanNet-1500 benchmark [30], which offers no semantic labels and we achieve the semantic prior by SEEM. Due to the data collection settings of MatterPort3D, image pairs with overlap in this dataset result in wide baseline and present challenging matching conditions. These conditions allow us to effectively showcase the performance of our method under difficult matching conditions. The KITTI360 dataset allows for the evaluation of driving scenes, which is a widely-used dataset for SLAM. The YFCC100M dataset contains internet images of architectural scenarios, which is also widely-used for feature matching.

B. Implementation Details

1) *Parameter Setting.* In the SAM, two semantic object areas with center distance (Sec. IV-A1) less than 100 pixels are fused. The parameter is set for sparse detection results. The multiscale ratios are [0.8, 1.2, 1.4] for the scale invariance enhancement of two area descriptors, which aim to achieve

more semantic specificity. The thresholds in *SOA* and *SIA* matching are set as $T_H = 0.5$, $T_L = 0.75$ and $T_{da} = 0.2$, which are smaller for more restricted matching. In *SIA* detection, the top layer reduce ratio in semantic pyramid is $r = 8$, which is a trade-off between detection efficient and accuracy. We empirically set the ϕ for T_{GR} as 0.5 for ScanNet and 1.0 for other datasets, the ablation study for which can be seen in Sec. V-G. The T_{SP} is set as 0.6 for ScanNet and 0.3 for other datasets, based on ablation study in Sec. V-H.

2) *Area Size*. The area size is the input size for the point matchers. In practice, the default area size is set as 256×256 for ScanNet, 480×480 for Matterport3D, YFCC, KITTI and 640×640 for ScanNet1500. For the matched semantic object areas (SOAs), the sizes are first expanded from the bounding boxes of objects to match the width-height ratio of the default size. Then the SOAs are cropped from the original images and resized to the default size before being entered into the point matcher. After matching, the correspondences outside the object bounding boxes are filtered out. For semantic intersection areas (SIAs), their size is related to the detection window, which is first set with the default size. To further mitigate the scale issue between images, we first match SOAs, which are robust to scale variation as the actual sizes of objects are fixed. Then, we adjust the detection windows of *SIA* in two images using the average size variation of *SOA* bounding boxes to obtain areas with consistent scales.

3) *Semantic Noise Filtering*. Our method takes semantic segmentation images as input, obtained from SOTA semantic segmentation methods or ground truth labels. However, even if provided with manual labels, these inputs can still contain semantic labeling errors. Thus, the semantic noise filtering needs to be performed in SAM. Specifically, in semantic object area detection, objects smaller than $1/100$ image size is ignored and the semantic surrounding descriptor neglects semantics with fewer than 20 continuous pixels at the boundary. In semantic intersection area detection, semantics smaller than $1/64$ window size are filtered. The semantic labels with size less than $1/64$ area size are filtered out in the construction of semantic proportion descriptor.

C. Point Matching

We conducted point matching experiments on ScanNet and MatterPort3D to evaluate matching precision. For ScanNet, we construct two matching difficulties with image pairs under various *Frame Differences* (FD@5/10), each including 1500 image pairs. For the more challenging matching condition, 500 image pairs are sampled from 5 scenes in MatterPort3D.

1) *Compared methods*. We compare the proposed A2PM framework with conventional matching frameworks including detector-based matching [5], [8], [9], [30] and detector-free matching [7], [10], [11], [37]. For A2PM framework, we combine SGAM with SOTA Transformer-based detector-free methods: SGAM_ASpan [7], SGAM_QuadT [11], SGAM_LoFTR [10] and SGAM_COTR [37]. To evaluate the robustness against semantic precision of our method, we provide our method with three kind of semantic segmentation source, i.e. the ground truth label (GT) and SOTA semantic

segmentation method SEEM [16] with two backbones: the **Large** FocalNet [47] (SEEM-L) and the **Tiny** one (SEEM-T). SEEM-L is more accurate than SEEM-T in semantic segmentation. For detector-free matching, we choose the original ASpan [7], QuadT [11], LoFTR [10] and COTR [37]. For detector-based matching, we select SuperPoint [5] with nearest neighbor matching (SP+NN) and with the learning matching SuperGlue [30] (SP+SG). The recent SOTA ASLFeat+NN [9] and ALike+NN [8] are compared as well.

2) *Evaluation protocol*. Following [8], [23], we report the Mean Matching Accuracy (MMA@i) in percentage under integer thresholds $i \in [1, 3]$ of each method and the number of matches is set as 500 for each method.

3) *Results*. The MMA values are reported in Tab. II, with improvement achieved by our methods are shown in percentage. It is evident that the SGAM significantly enhances the matching precision of all detector-free methods. It is worth noting that ScanNet serves as the training dataset for ASpan, QuadT, and LoFTR. Despite this, SGAM still demonstrates impressive accuracy improvement for these methods. On MatterPort3D dataset, SGAM exhibits substantial precision improvement and outperforms other methods by a noteworthy margin, thus underscoring the superiority of SGAM in challenging matching scenarios. Overall, our method consistently achieves significant improvements under various matching difficulties, highlighting the robustness and effectiveness of our approach. For each baseline, Tab. II also presents a comparison of different semantic inputs of our method. The ground truth labels are most precise, while SEEM, trained with COCO [48] labels, may introduce unidentified objects, resulting in a slight decrease in precision. SGAM using SEEM-L gets higher accuracy than using SEEM-T, demonstrating the matching accuracy increases with the semantic segmentation precision. Nevertheless, the semantic prior provided by the current semantic segmentation method is sufficient for our approach to achieve remarkable accuracy improvements in matching tasks. In sum, owing to the proper search space, which alleviates many matching challenges and provides high-resolution input for point matcher, SGAM notably improves the matching accuracy for SOTA detector-free matchers. We offer the visualization of qualitative results in Fig. 11.

D. Relative Pose Estimation

Accurate matches do not necessarily lead to accurate geometry, where point distribution is also important. Thus we next evaluate our method for relative pose estimation. The dataset used in our evaluation comprises both indoor and outdoor scenes. Specifically, we employ ScanNet and Matterport3D for indoor scenes. We sample 2×1500 image pairs from ScanNet (FD@5/10) and 500 image pairs from MatterPort3D to construct three difficulties. We also investigate the influence of different semantic inputs. Additionally, we compare our method with more SOTA methods [14], [15], [32], [40], [49]–[51] on the standard ScanNet-1500 benchmark [30], using SEEM-L to obtain the semantic segmentation results. Due to the *static world assumption* [1], [2] in our downstream tasks, we utilized three sequences in the KITTI360 dataset (Seq. 00,

TABLE III

RELATIVE POSE ESTIMATION RESULTS (%). THE AUC OF POSE ERROR ON SCANNET (FD@5/10) AND MATTERPORT3D WITH DIFFERENT THRESHOLDS ARE REPORTED. **OUR SGAM** IS APPLIED ON FOUR BASELINES. TO SHOW THE IMPACT OF SEMANTIC ACCURACY TO OUR METHOD, WE TAKES THREE DIFFERENT SEMANTIC INPUTS: **SGAM USING GROUND TRUTH (GT)**, **SGAM USING SEEM-L** AND **SGAM USING SEEM-T**. THE IMPROVEMENT ACHIEVED BY SGAM IS ALSO REPORTED IN PERCENTAGE.

Pose estimation AUC	ScanNet: FD@5			ScanNet: FD@10			MatterPort3D		
	AUC@5°↑	AUC@10°↑	AUC@20°↑	AUC@5°↑	AUC@10°↑	AUC@20°↑	AUC@10°↑	AUC@20°↑	AUC@30°↑
SP [5]+NN	63.07	70.83	85.41	53.19	64.46	73.99	13.82	24.09	35.26
SP [5]+SG [30]	67.46	76.46	86.61	53.11	64.47	73.58	16.39	29.54	37.61
ASLFeat [9]+NN	68.08	75.64	85.66	56.89	68.66	78.33	12.64	25.91	39.26
ALike [8]+NN	69.67	78.29	83.46	50.29	61.27	70.31	15.14	20.03	23.79
ASpan [7]	70.73	77.41	80.19	58.51	70.42	79.84	18.35	27.81	43.98
GT+SGAM_ASpan	73.60 ^{+4.06%}	81.52 ^{+5.30%}	85.83 ^{+7.02%}	60.78 ^{+3.89%}	74.24 ^{+5.43%}	84.53 ^{+5.87%}	20.50 ^{+11.71%}	30.08 ^{+8.17%}	48.49 ^{+10.26%}
SEEM-L [16]+SGAM_ASpan	72.32 ^{+3.24%}	80.59 ^{+4.10%}	85.20 ^{+6.24%}	59.17 ^{+1.13%}	73.02 ^{+3.69%}	83.40 ^{+4.46%}	19.74 ^{+7.56%}	29.38 ^{+5.66%}	45.52 ^{+3.51%}
SEEM-T [16]+SGAM_ASpan	71.84 ^{+1.56%}	79.94 ^{+3.26%}	83.32 ^{+3.90%}	58.87 ^{+0.62%}	72.02 ^{+2.27%}	82.54 ^{+3.38%}	18.64 ^{+1.56%}	28.87 ^{+3.81%}	44.34 ^{+0.83%}
QuadT [11]	69.48	74.25	79.39	59.27	69.77	74.96	16.53	26.98	39.96
GT+SGAM_QuadT	72.55 ^{+4.41%}	75.89 ^{+2.27%}	82.10 ^{+3.41%}	61.82 ^{+4.31%}	71.83 ^{+2.95%}	76.82 ^{+2.49%}	18.90 ^{+14.33%}	28.11 ^{+4.19%}	42.21 ^{+5.63%}
SEEM-L [16]+SGAM_QuadT	71.92 ^{+3.51%}	75.60 ^{+1.81%}	81.43 ^{+2.56%}	61.78 ^{+4.23%}	71.96 ^{+3.14%}	76.52 ^{+2.08%}	17.83 ^{+7.82%}	27.25 ^{+1.00%}	41.56 ^{+4.00%}
SEEM-T [16]+SGAM_QuadT	71.47 ^{+2.86%}	75.06 ^{+1.09%}	80.66 ^{+1.59%}	60.97 ^{+2.87%}	71.77 ^{+2.86%}	75.80 ^{+1.13%}	16.84 ^{+1.88%}	27.10 ^{+0.44%}	40.22 ^{+0.65%}
LoFTR [10]	67.69	74.29	78.45	58.71	69.81	78.99	17.98	27.79	38.19
GT+SGAM_LoFTR	71.22 ^{+5.21%}	79.31 ^{+6.76%}	84.44 ^{+7.64%}	59.50 ^{+1.35%}	73.12 ^{+4.74%}	83.13 ^{+5.24%}	18.14 ^{+0.89%}	32.28 ^{+16.16%}	45.37 ^{+18.80%}
SEEM-L [16]+SGAM_LoFTR	70.25 ^{+3.79%}	79.23 ^{+6.65%}	83.93 ^{+6.99%}	60.37 ^{+2.83%}	71.02 ^{+1.74%}	80.91 ^{+2.42%}	18.04 ^{+0.31%}	30.86 ^{+11.04%}	42.13 ^{+10.32%}
SEEM-T [16]+SGAM_LoFTR	69.53 ^{+2.72%}	78.03 ^{+5.03%}	82.32 ^{+4.93%}	59.01 ^{+0.50%}	70.58 ^{+1.10%}	79.78 ^{+1.01%}	17.47 ^{-2.85%}	30.00 ^{+7.94%}	40.63 ^{+6.39%}
COTR [37]	66.91	74.11	78.48	51.92	63.36	72.55	17.80	25.08	34.08
GT+SGAM_COTR	71.18 ^{+6.38%}	79.22 ^{+6.90%}	84.22 ^{+7.31%}	53.99 ^{+3.99%}	68.29 ^{+7.78%}	80.17 ^{+10.50%}	19.20 ^{+7.87%}	28.31 ^{+12.88%}	41.25 ^{+21.04%}
SEEM-L [16]+SGAM_COTR	69.67 ^{+4.12%}	78.15 ^{+5.46%}	83.84 ^{+6.83%}	52.80 ^{+1.70%}	66.16 ^{+4.42%}	78.78 ^{+8.59%}	18.12 ^{+1.82%}	26.99 ^{+7.62%}	36.69 ^{+7.67%}
SEEM-T [16]+SGAM_COTR	69.40 ^{+3.72%}	77.98 ^{+5.32%}	83.07 ^{+5.85%}	52.07 ^{+0.28%}	65.91 ^{+4.03%}	78.43 ^{+8.10%}	17.93 ^{+0.71%}	25.79 ^{+2.84%}	35.79 ^{+5.01%}

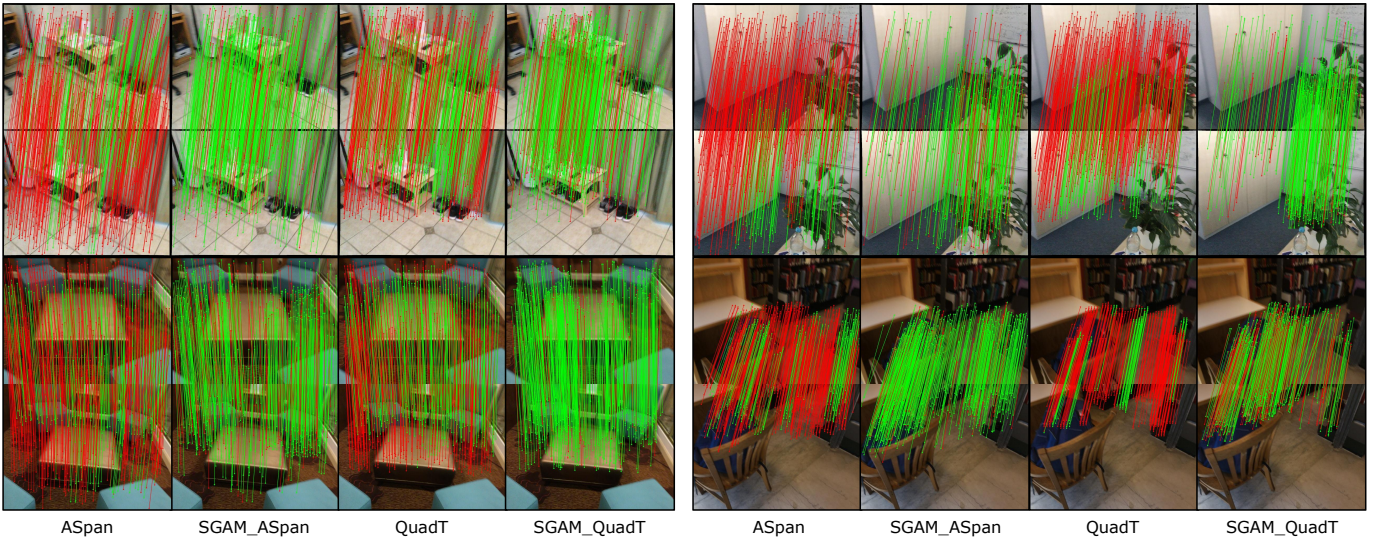


Fig. 4. **Qualitative Comparison on ScanNet**. The visual comparison between our method and two SOTA baselines. The **wrong** and **correct** matches under the same threshold are labeled respectively. The point matches we obtained possess much higher precision as well as uniform distribution.

03 and 05) with few moving objects, like pedestrians, for pose estimation estimation. In these sequences, we showcase the improvement achieved by our method across four baselines, using the semantic prior from both ground truth and SEEM-L results. For YFCC100M [46] dataset, we follow the previous work [30], [52] to construct pose estimation evaluation with 4k image pairs. We also use SEEM-L and SEEM-T to obtain semantic prior of this dataset for our method.

1) *Evaluation protocol*. Following [10], [30], we report the pose estimation AUC. The camera pose is recovered by solving the essential matrix with RANSAC. Correspondences are uniformly sampled from the image, with a maximum number of 500. For ScanNet, KITTI360 and YFCC100M dataset, we report the pose AUC@5°/10°/20°. As pose estimation is hard in MatterPort3D, we report the pose AUC@10°/20°/30°. The comparison methods includes those in point matching

experiments and other recent SOTA methods [14], [52].

2) *Indoor Results*. The pose AUC results in indoor scene are summarised in Tab. III and Tab. V. It is evident that our method significantly improves performance across all baselines, attributable to both enhanced matching accuracy and the even matching distribution. Particularly noteworthy is the impressive precision improvement achieved on the challenging MatterPort3D dataset, underscoring the superiority of our method in tackling difficult matching scenarios. Furthermore, similar to the point matching experiment, higher semantic precision leads to improved geometry estimation. The recent SEEM is able to offer enough accurate semantic prior for our method, even it is trained with COCO [48] labels. Additionally, in Table V, we compare our method with other leading matching approaches on the standard ScanNet-1500 benchmark. Since this benchmark lacks semantic labels, we

TABLE IV
RELATIVE POSE ESTIMATION RESULTS (%) ON KITTI360 DATASET. WE COMPARE TWO DIFFERENT SEMANTIC INPUTS FOR OUR METHOD:
SGAM USING GROUND TRUTH (GT) AND SGAM USING SEEM-L.

Pose estimation AUC	Seq. 00			Seq. 03			Seq. 05		
	AUC@5°↑	AUC@10°↑	AUC@20°↑	AUC@5°↑	AUC@10°	AUC@20°↑	AUC@10°↑	AUC@20°↑	AUC@30°↑
A_Span [7]	61.19	77.64	87.95	68.01	83.00	91.20	57.38	75.57	87.16
GT+SGAM_A_Span	66.05 ^{+7.95%}	81.86 ^{+5.44%}	90.63 ^{+3.05%}	73.81 ^{+8.53%}	86.43 ^{+4.14%}	92.96 ^{+1.94%}	63.31 ^{+10.35%}	80.22 ^{+6.15%}	89.78 ^{+3.00%}
SEEM-L [16]+SGAM_A_Span	66.18 ^{+8.17%}	81.67 ^{+5.19%}	90.38 ^{+2.76%}	73.70 ^{+8.46%}	86.40 ^{+4.10%}	92.95 ^{+1.92%}	63.06 ^{+9.91%}	80.07 ^{+5.95%}	89.70 ^{+2.92%}
QuadT [11]	59.93	77.77	88.27	66.47	81.81	90.39	58.93	77.24	88.40
GT+SGAM_QuadT	67.77 ^{+13.10%}	82.68 ^{+6.32%}	91.04 ^{+3.13%}	73.40 ^{+10.42%}	86.05 ^{+5.18%}	92.68 ^{+2.53%}	65.98 ^{+11.96%}	81.97 ^{+6.11%}	90.83 ^{+2.75%}
SEEM-L [16]+SGAM_QuadT	67.72 ^{+13.01%}	82.63 ^{+6.25%}	91.01 ^{+3.10%}	73.33 ^{+10.32%}	86.00 ^{+5.12%}	92.65 ^{+2.51%}	65.92 ^{+11.86%}	81.77 ^{+5.86%}	90.67 ^{+2.57%}
LoFTR [6]	65.11	80.98	90.10	71.53	84.87	92.11	63.54	80.19	89.95
GT+SGAM_LoFTR	70.55 ^{+8.36%}	84.79 ^{+4.71%}	92.33 ^{+2.48%}	75.40 ^{+5.41%}	86.95 ^{+2.45%}	93.03 ^{+1.00%}	69.68 ^{+9.66%}	84.44 ^{+5.30%}	92.20 ^{+2.50%}
SEEM-L [16]+SGAM_LoFTR	70.20 ^{+7.83%}	84.54 ^{+4.39%}	92.16 ^{+2.29%}	76.21 ^{+6.54%}	87.27 ^{+2.83%}	93.18 ^{+1.16%}	69.51 ^{+9.39%}	84.11 ^{+4.89%}	92.01 ^{+2.29%}
COTR [37]	62.76	77.61	86.67	66.97	80.92	89.22	58.69	79.36	88.55
GT+SGAM_COTR	67.55 ^{+7.63%}	81.70 ^{+5.27%}	88.30 ^{+1.89%}	72.40 ^{+8.11%}	85.89 ^{+6.15%}	91.32 ^{+2.35%}	66.17 ^{+12.75%}	82.01 ^{+3.34%}	90.96 ^{+2.72%}
SEEM-L [16]+SGAM_COTR	66.69 ^{+6.26%}	80.90 ^{+4.23%}	88.37 ^{+1.96%}	70.17 ^{+4.77%}	84.21 ^{+4.07%}	90.17 ^{+1.06%}	64.39 ^{+9.72%}	81.19 ^{+2.31%}	90.18 ^{+1.85%}

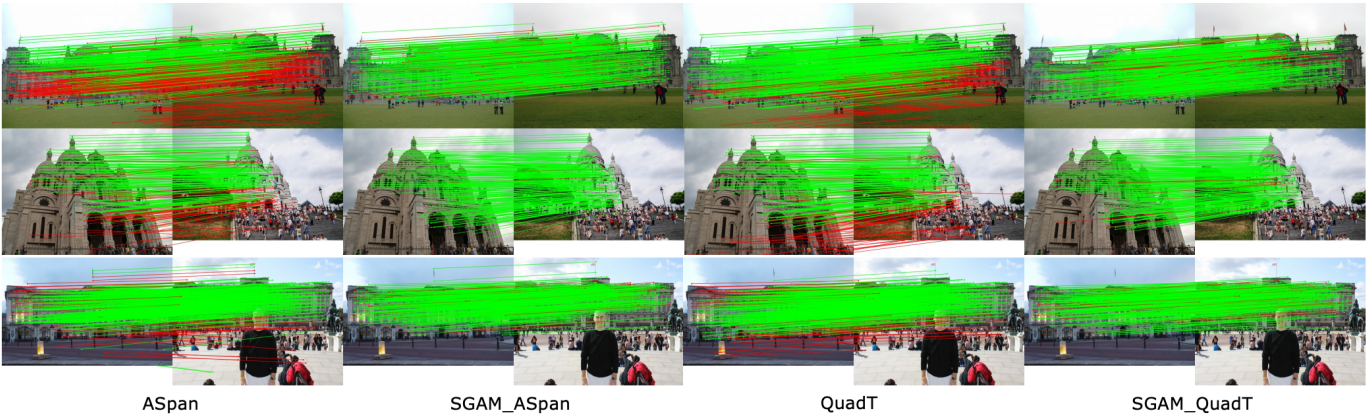


Fig. 5. Qualitative Comparison on YFCC100M. The visual comparison between our method and two SOTA baselines. The wrong and correct matches under the same threshold are labeled respectively.

TABLE V
RELATIVE POSE ESTIMATION RESULTS (%) ON SCANNET-1500 BENCHMARK. OUR METHOD OBTAINS THE SEMANTIC PRIOR BY SEEM-L. THE BEST AND SECOND RESULTS ARE HIGHLIGHTED.

Pose estimation AUC	ScanNet-1500 benchmark		
	AUC@5°↑	AUC@10°↑	AUC@20°↑
SP [5]+OANet [32]	11.80	26.90	43.90
SP+SGMNet [49]	15.40	32.10	48.30
SP+SG [30]	16.20	33.80	51.80
SP+SG+MKPC [14]	16.18 ^{-0.12%}	34.11 ^{+0.92%}	52.47 ^{+1.29%}
DRC-Net [50]	7.70	17.90	30.50
MatchFormer [51]	24.30	43.90	61.40
PATS [15]	26.00	46.90	64.30
A_Span [7]	25.78	46.14	63.32
SEEM-L [16]+SGAM_A_Span	27.51 ^{+6.71%}	48.01 ^{+4.05%}	65.26 ^{+3.06%}
QuadT [11]	25.21	44.85	61.70
SEEM-L+SGAM_QuadT	25.53 ^{+1.27%}	46.02 ^{+2.60%}	63.40 ^{+2.76%}
LoFTR [6]	22.13	40.86	57.65
SEEM-L+SGAM_LoFTR	23.39 ^{+5.69%}	41.79 ^{+2.28%}	58.74 ^{+1.89%}
DKM [40]	29.40	50.74	68.31
SEEM-L+SGAM_DKM	30.61 ^{+4.12%}	52.34 ^{+3.10%}	69.31 ^{+1.48%}

employ SEEM-L to perform semantic segmentation for our method. In this experiment, we further combine SGAM with a dense matching method, DKM [40], whose performance is also significantly boosted by our approach. The results demonstrate that our method outperforms other approaches by a considerable margin, achieving the highest accuracy

TABLE VI
RELATIVE POSE ESTIMATION RESULTS (%) ON YFCC100M. TWO DIFFERENT SEMANTIC INPUTS FOR OUR METHOD ARE COMPARED: SGAM USING SEEM-L AND SGAM USING SEEM-T. THE BEST AND SECOND RESULTS ARE HIGHLIGHTED.

Pose estimation AUC	YFCC100M		
	AUC@5°↑	AUC@10°↑	AUC@20°↑
SP [5]+NN	16.49	30.39	45.27
SP+OANet [32]	26.82	45.04	62.17
SP+SceneFM [52]	31.45	52.27	70.31
SP+SG [30]	28.45	48.6	67.19
SP+SG+MKPC [14]	37.73 ^{+19.97%}	58.03 ^{+11.02%}	74.57 ^{+6.06%}
A_Span [7]	38.96	59.35	75.54
SEEM-L [16]+SGAM_A_Span	39.90 ^{+2.41%}	60.36 ^{+1.70%}	76.34 ^{+1.06%}
SEEM-T [16]+SGAM_A_Span	39.77 ^{+2.08%}	60.24 ^{+1.50%}	76.21 ^{+0.89%}
QuadT [11]	40.73	61.19	76.57
SEEM-L+SGAM_QuadT	41.32 ^{+1.45%}	61.33 ^{+0.23%}	76.79 ^{+0.29%}
SEEM-T+SGAM_QuadT	41.07 ^{+0.83%}	61.44 ^{+0.41%}	77.02 ^{+0.58%}
LoFTR [10]	41.12	61.43	77.01
SEEM-L+SGAM_LoFTR	41.54 ^{+0.95%}	61.72 ^{+0.47%}	77.12 ^{+0.14%}
SEEM-T+SGAM_LoFTR	41.33 ^{+0.51%}	61.67 ^{+0.39%}	77.08 ^{+0.09%}
COTR [37]	39.73	59.12	74.27
SEEM-T+SGAM_COTR	39.94 ^{+0.53%}	60.89 ^{+2.99%}	74.65 ^{+0.51%}
SEEM-L+SGAM_COTR	40.19 ^{+1.16%}	60.31 ^{+1.97%}	74.76 ^{+0.66%}

and highlighting its effectiveness in practical applications. In particular, there is another two-stage matching method similar to our method, MKPC [14], which achieves co-visible area to match by stage-one point matching. However, its accuracy

TABLE VII

AREA MATCHING PERFORMANCE ON SCANNET. THE AREA MATCHING RESULTS (%) OF SAM AND SGAM COMBINED WITH DIFFERENT POINT MATCHERS UNDER THREE MATCHING DIFFICULTIES AND THREE SEMANTIC INPUT SETTINGS IN SCANNET ARE REPORTED. THE BEST AND SECOND RESULTS UNDER EACH SEMANTIC INPUT SETTING ARE HIGHLIGHTED.

Semantic		GT					SEEM-L					SEEM-T				
Method		SAM		SGAM			SAM		SGAM			SAM		SGAM		
Point	Matcher	-	ASpan	QuadT	LoFTR	COTR	-	ASpan	QuadT	LoFTR	COTR	-	ASpan	QuadT	LoFTR	COTR
FD@5	AOR↑	84.95	89.54	91.40	<u>90.03</u>	89.41	85.12	85.27	86.18	<u>86.14</u>	85.31	78.70	79.30	<u>80.43</u>	80.69	79.34
	AMP@0.7↑	89.42	93.43	98.45	<u>94.35</u>	92.43	87.26	96.43	<u>89.28</u>	88.98	87.47	77.44	79.27	<u>80.32</u>	80.44	80.01
FD@10	AOR↑	84.38	84.52	87.69	<u>85.46</u>	84.62	80.08	80.16	82.34	81.28	80.93	72.84	74.38	74.80	74.80	73.49
	AMP@0.7↑	88.71	92.87	97.57	<u>93.07</u>	89.25	79.07	85.52	<u>82.08</u>	81.51	80.52	67.28	68.95	69.16	69.84	<u>69.30</u>
FD@30	AOR↑	69.46	72.29	79.95	<u>72.56</u>	70.03	69.97	71.75	<u>72.80</u>	72.95	70.23	61.84	64.85	<u>65.37</u>	65.82	65.34
	AMP@0.7↑	75.32	80.56	88.41	<u>82.15</u>	76.72	58.52	64.05	<u>62.68</u>	<u>63.04</u>	60.51	45.49	47.72	<u>48.51</u>	48.91	47.34

gains for the baseline is very limited. This limitation may be attributed to the fact that MKPC can only achieve single area match for each pair of images. Moreover, its area matching accuracy is dependent on precise point matching, which is challenging to achieve in complex indoor scenes. In contrast, SGAM is particularly well-suited for indoor scenes due to their abundance of semantic information, making it more effective in this context.

3) *Outdoor Results.* The results on KITTI360 dataset are reported in Tab. IV. Our method greatly enhances the precision of pose estimation for all baselines, affirming the effectiveness and robustness of our method in outdoor driving scenes. It is important to highlight that the impact of different semantic inputs on performance is minimal here. This is primarily due to the reduced semantic complexity of driving scenes compared to indoor scenes, wherein the SEEM-L backbone can yield accurate semantic segmentation outcomes. Thus, SGAM demonstrates the capability to achieve precise pose estimation when SEEM is employed to obtain semantic prior, thereby showcasing the practicality of our approach.

The Tab. VI reports the results on YFCC100M dataset. Similar to indoor experiments, we obtain semantic input using SEEM with two backbones to study the impact of different semantic inputs on performance. As we can see in this table, our SGAM is able to boost the performance for all baselines. However, the improvements in this outdoor scene are limited (up to +2.41%), compared to indoor and driving scenes. The underlying reason is that the semantic information in this scene is very limited, leading to semantic segmentation at large granularity, e.g. segmentation only contains labels like ‘sky’, ‘building’ and ‘people’. Thus, SGAM attains few area matches, usually covering almost the whole image, and therefore has limited advantages for subsequent point matching. In contrast, MKPC is more suitable to this dataset and achieves more improvement. However, SGAM does outperform MKPC in accuracy, combined with all baselines. Additionally, we provide some qualitative comparison examples in Fig. 5, where the accuracy of our SGAM against the baselines is improved.

E. Area Matching

We also evaluate SGAM on ScanNet dataset [43] for area matching performance. We sample 3×1500 image pairs for three matching difficulties (FD@5/10/30) in ScanNet. The impact of semantic precision for area matching is investigated

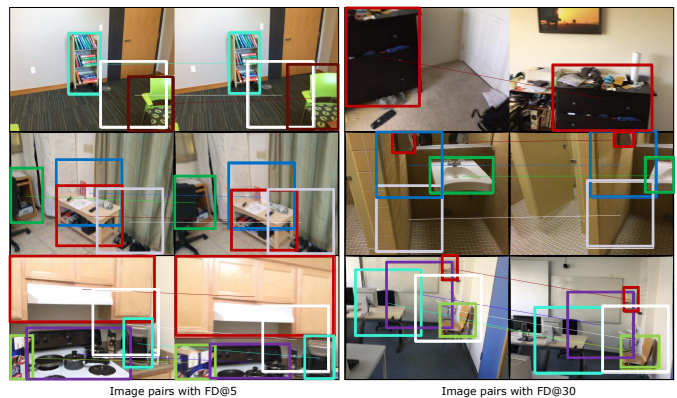


Fig. 6. **Qualitative Results of Area Matching.** We show the area matching results of SGAM on ScanNet dataset, using image pairs with two frame differences (FD@5 and FD@30). Each area match is indicated by a box pair with the same color. Two kinds of semantic areas can be seen in these cases, i.e. the semantic object areas centered in objects and the semantic intersection areas between objects, covering most of the overlap.

using three semantic input (GT and SEEM-L/T). Furthermore, we compare the performance of SAM alone with that of SGAM integrated with different point matchers.

1) *Evaluation protocol.* To measure the area matching accuracy, we propose two area matching metrics as follows.

(a) **Area Overlap Ratio (AOR).** This metric is to evaluate the single area match accuracy and achieved by projecting points $\{\{p_i\}_i^N\}$ of $\alpha \in I_0$ to I_1 and getting the proportion of points falling into the matched area $\beta \in I_1$.

$$AOR(A) = \frac{1}{N} \sum_i^N (C(P(p_i), \beta)) \tag{15}$$

where the area match $A = (\alpha, \beta)$, $P(p_i)$ is projecting point p_i to I_1 , $C(q_i, \beta)$ is 1 when $q_i \in \beta$, otherwise 0.

(b) **Area Matching Precision@t (AMP@t).** Given all area matches $\{\mathcal{A}_{i,\pi(i)}\}_i^M$ and a specific threshold $t \in [0, 1]$, this metric is the proportion of area matches whose $AOR > t$, evaluating the overall matching accuracy.

$$AMP@t = \frac{1}{M} \sum_i^M F(\mathcal{A}_{i,\pi(i)}, t) \tag{16}$$

where $F(\mathcal{A}_{i,\pi(i)}, t)$ is 1 when $AOR(\mathcal{A}_{i,\pi(i)}) > t$, otherwise 0.

2) *Results.* The area matching results are summarised in Tab. VII. The threshold t of AMP is set as 0.7. We

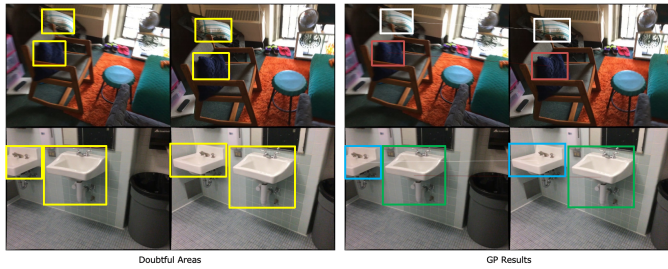


Fig. 7. **Visualization of GP.** The cases processed by GP, which can predict the true matches (boxes of the same color) from the doubtful candidates (yellow boxes) in semantic ambiguity.

analyze the outcomes of SAM and SGAM when combined with SOTA detector-free matchers. Within the table, the precision of area matching in SAM decreases as the matching difficulty increases. When the semantic input is accurate (GT), the AMP values demonstrate that most areas are accurately matched under all conditions. However, as semantic precision decreases, our method also experiences a decrease in precision, which is more pronounced in large FD. This demonstrates the main limitation of our method, i.e. the heavy reliance on semantic, which is discussed in detail in Sec. V-K. Notably, the utilization of SGAM enhances the accuracy of area matching in all scenarios, highlighting the importance of GAM in area matching. Different point matchers also result in different regional matching precision, but the overall difference is small, proving the compatibility of our method for point matchers.

F. Understanding SAM

SAM contains matching two kinds of areas: the semantic object area (SOA) and the semantic intersection area (SIA). To assess the importance of these two areas on area matching, we designed experiments to evaluate their quantities and matching accuracy in ScanNet image pairs with FD@5/10/30. To further investigate the performance under different semantic input accuracy, SAM takes three semantic segmentation as input, including ground truth (GT sem.) and segmentation by SEEM with two backbones (SEEM-L/T Sem.). The results are summarised in the Tab. VIII, including the **SOA Match** and **SIA Match** under different FD and semantic input. It can be seen that SOA matches are more accurate and robust against semantic precision compared to SIA. This can be attributed to the better stability of the centered object semantic against various matching noises. On the other hand, the precision of SAM is limited by semantic precision. As shown in the table, the accuracy of area matching decreases with semantic accuracy, and the decrease is more significant at large FD. This limitation is discussed in detail in Sec. V-K. In addition, both two areas are frequently involved in the matching and sufficient number of area matches is also important for downstream tasks, indicating their importance for SGAM.

G. Understanding GAM

1) *GP Precision.* This section focuses on examining the area matching performance of GP on ScanNet [43] across three difficulty levels and semantic input (GT and SEEM-T/L), each consisting of 1500 image pairs. The results are shown in

TABLE VIII
AREA MATCHING PERFORMANCE ON SCANNET OF TWO SAM AREAS AND GP. WE CONSTRUCT AREA MATCHING EXPERIMENTS FOR MATCHING OF TWO SEMANTIC AREAS, ALONG WITH GP INTEGRATED WITH FOUR POINT MATCHERS. THE EFFECT OF THREE DIFFERENT SEMANTIC INPUTS ON PERFORMANCE IS TESTED. AOR AND AMP (WITH THRESHOLD $t = 0.7$) UNDER DIFFERENT MATCHING DIFFICULTIES (EACH WITH 1500 IMAGE PAIRS) ARE REPORTED ALONG WITH THE AREA NUMBER PER IMAGE (NUM). THE **BEST** AND **SECOND** RESULTS UNDER EACH SEMANTIC INPUT SETTING AND FD SETTING ARE HIGHLIGHTED.

Method	FD@5			FD@10			FD@30			
	AOR↑	AMP↑	Num	AOR↑	AMP↑	Num	AOR↑	AMP↑	Num	
GT Sem.	SOA Match	85.94	94.10	3.13	85.26	91.76	2.91	70.84	68.36	2.30
	SIA Match	83.67	91.91	2.38	83.50	84.35	2.01	66.94	62.17	1.26
	GP_ASpan	86.59	96.70		84.83	89.59		81.26	86.97	
	GP_QuadT	87.86	96.82		84.98	88.47		82.37	87.91	
	GP_LoFTR	87.51	95.73	0.26	87.42	92.18	0.36	73.81	86.48	0.50
GP_COTR	86.46	95.27		86.58	89.37		73.12	82.59		
SEEM-L Sem.	SOA Match	86.33	89.94	3.35	81.14	81.22	4.94	72.25	62.74	2.62
	SIA Match	83.39	83.46	2.51	77.19	72.53	2.21	65.85	51.01	1.76
	GP_ASpan	84.90	90.66		83.34	84.51		75.43	63.02	
	GP_QuadT	85.03	87.26		81.54	82.06		74.03	63.16	
	GP_LoFTR	87.23	89.94	0.57	82.59	83.91	0.64	74.25	64.44	1.61
GP_COTR	85.39	89.65		80.73	81.54		73.87	63.48		
SEEM-T Sem.	SOA Match	80.97	81.31	3.78	75.12	71.21	3.37	63.73	47.10	2.69
	SIA Match	70.57	63.49	1.82	64.13	52.23	1.63	53.70	38.45	1.47
	GP_ASpan	81.39	83.19		77.17	73.19		64.89	48.93	
	GP_QuadT	81.09	82.79		77.59	72.38		64.36	48.76	
	GP_LoFTR	81.74	82.91	0.77	77.45	72.12	1.15	64.29	48.59	1.60
GP_COTR	81.59	82.63		76.93	71.61		64.17	48.15		

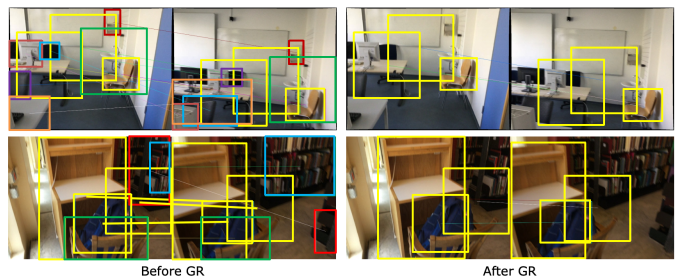


Fig. 8. **Visualization of GR.** After GR, many false and inaccurate area matches (boxes of the same color) are rejected. Only reliable area matches (highlighted by yellow boxes) are left, leading to high matching accuracy for point matching.

Tab. VIII. It can be seen that the area matching precision of GP surpasses that of SAM under different matching difficulties. Similar to SAM, the precision of GP decreases with inaccurate semantic input, but it can establish more accurate area matches than SAM in all semantic input cases. These observations confirm the effectiveness of GP. Furthermore, the choice of point matchers influences the performance of GP, with improved point matching leading to increased accuracy in area matching. Notably, the doubtful area count per image indicates non-trivial semantic ambiguity within SAM, which becomes more prevalent with increasing matching difficulty. In conclusion, GP plays a crucial role in SGAM by addressing semantic ambiguity and enhancing area matching performance. The visualization of GP are shown in Fig. 7.

2) *Ablation Study of GR Parameter.* In order to thoroughly examine the influence of the parameter ϕ in GR on pose estimation performance, we conduct experiments on ScanNet. We evaluate two difficulty levels, FD@10 and FD@30, each consisting of 1500 image pairs. The obtained results are depicted in Fig. 9. It is evident that the choice of ϕ has minimal impact when the frame difference is 10. In scenes where the matching difficulty is not too high, an adequate

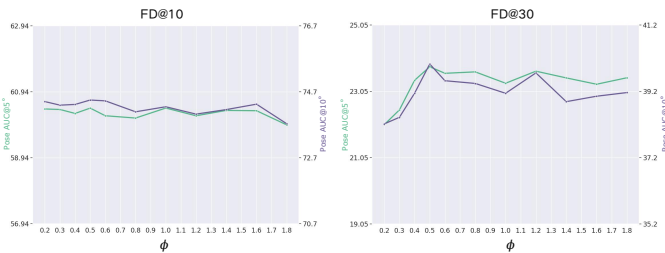


Fig. 9. **Ablation study of GR parameter ϕ .** We report the pose estimation performance ($AUC@5^\circ/10^\circ$) of SGAM_ASpan with various ϕ settings on ScanNet dataset under FD@10 (left) and FD@30 (right). Although smaller ϕ brings more accurate area matches, it also aggregates point matches together which may result in planar degradation. Setting ϕ appropriately, therefore, is important especially in difficult matching scenes.

TABLE IX

COMPARISON EXPERIMENT ON MAXIMUM CORRESPONDENCE NUMBER (MCN). THE POSE ESTIMATION RESULTS ON SCANNET WITH FD@10 AND YFCC100M ARE REPORTED. OUR METHOD IS COMBINED WITH ASPAN AND TAKES SEMANTIC INPUT FROM SEEM-T. WE SHOW THE IMPROVEMENT OF OUR METHOD ON THE ACCURACY OF ASPAN.

MCN	Method	ScanNet-FD@10			YFCC100M		
		AUC@5°↑	AUC@10°↑	AUC@20°↑	AUC@5°↑	AUC@10°↑	AUC@20°↑
500	ASpan	58.51	70.42	79.84	38.96	59.35	75.54
	SGAM_ASpan	60.78 _{+3.88%}	74.24 _{+5.42%}	84.53 _{+5.87%}	39.77 _{+2.08%}	60.24 _{+1.50%}	76.21 _{+0.89%}
800	ASpan	58.02	68.45	78.41	39.35	59.72	75.67
	SGAM_ASpan	60.36 _{+4.38%}	71.17 _{+3.97%}	79.84 _{+1.82%}	40.05 _{+1.78%}	60.53 _{+1.36%}	76.34 _{+1.15%}
1000	ASpan	57.81	67.66	77.59	39.18	59.54	75.60
	SGAM_ASpan	60.24 _{+4.20%}	72.65 _{+7.38%}	80.77 _{+4.10%}	40.55 _{+3.50%}	60.84 _{+2.18%}	76.78 _{+1.56%}

number of area matches are identified. With a smaller ϕ value, accurate area matches are selected, (thanks to our GMC module which ensures the even distribution of matches) leading to improved performance. However, as the difficulty of area matching increases under FD@30, a smaller ϕ value can cause point matches to be spatially concentrated, resulting in planar degeneration in certain cases. Hence, selecting an appropriate ϕ is crucial in challenging matching scenarios. Based on empirical findings, we establish $\phi = 0.5$ as the default value. We visualize the GR in Fig. 8.

H. Understanding Global Match Collection

Global Match Collection (GMC) is another important module of our method, which ensures widely distributed point matches, particularly in less semantic scenes. To demonstrate the contribution of this module in our method, we conducted an ablation study on the ScanNet-1500 benchmark. The results are summarised in Fig. 10. The main parameter of our study is the size proportion threshold (T_{SP}), which represents the proportion of the image occupied by matched areas in the image pair. When $T_{SP} = 0$, no GMC is performed, and when $T_{SP} = 1$, all image pairs adopt the GMC module. First, we demonstrate the relationship between T_{SP} and the collection proportion, which represents the percentage of cases that adopt the GMC among all the pairs (Fig. 10(a)). The relationship is close to linear, which is consistent with common sense. Next, we display the pose estimation performance ($AUC@5^\circ/10^\circ$) under different size proportion thresholds (Fig. 10(b)). In the figure, the performance increases significantly as the threshold changes from 0.1 to 0.3. This is because the GMC module can significantly improve the distribution of matches, especially when there are only a few area matches established. It is

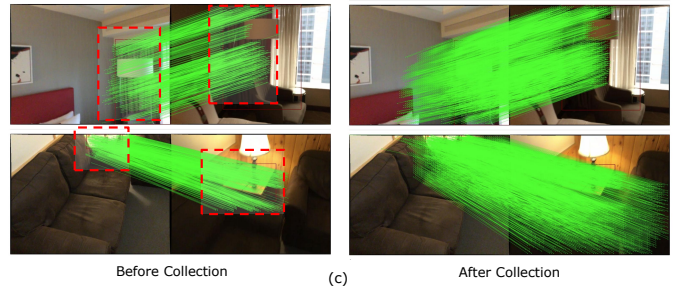
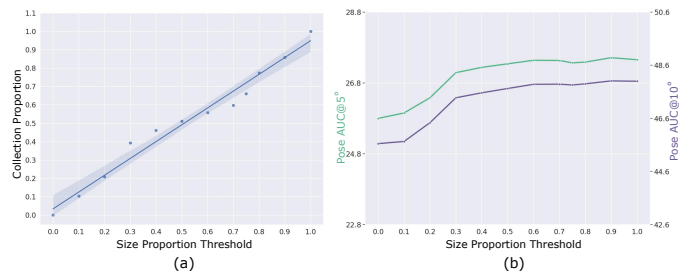


Fig. 10. **Ablation study of global match collection.** We conduct the ablation study to evaluate the effectiveness of global match collection module on the ScanNet-1500 benchmark. (a) The relationship between the size proportion threshold and the number of cases using the global match collection module (collection proportion). (b) The relationship between the size proportion threshold and the pose estimation precision ($Pose AUC@5^\circ/10^\circ$). (c) The qualitative cases before and after global match collection. The red dash boxes indicate the area matches.

worth noting that even without GMC, our method can slightly improve the precision of the baseline ($AUC@5^\circ$: 25.89 vs. 25.78). However, the GMC module brings better performance. As the threshold further increases, the performance improvement levels off because the area matches already cover most of the overlap in the image pair. Therefore, to achieve better performance while considering the computation cost of the GMC module (equal to one area match with images resized to the default size), the size proportion threshold can be set to 0.6. Moreover, we visualize the affects of GMC in Fig. 10 (c), where the distribution of matches is more uniform in the overlap area after applying GMC. Another concern about GMC is that it achieves more but may be duplicate correspondences, due to the overlaps between area matches and GMC. However, as we uniformly sample no more than the *Maximum Correspondence Number* (MCN) of points in the image space for pose estimation, duplicate correspondences are removed. Additionally, we conduct experiments on both ScanNet (FD@10, 1.5k image pairs) and YFCC100M, to investigate the influence of the MCN on the pose estimation, which is set as 500, 800 and 1000 respectively. The results are reported in Table IX. It is evident that the MCN have slight impact on pose estimation and SGAM demonstrates improvement across all settings.

I. Decomposing Ablation Study

We also conducted a dedicated experiment to systematically decompose the components of our approach, evaluating the area matching and pose estimation performance. The threshold of AMP is set as $t = 0.7$. We sample 1500 image pair with frame difference is 15 (FD@15) from ScanNet for this experiment. Our SGAM is combined with ASpan. The results

TABLE X

DECOMPOSING COMPONENT ABLATION STUDY. WE CONDUCT THE DECOMPOSING COMPONENT EXPERIMENT OF SGAM_ASPAN ON SCANNET WITH FD@15, USING 1K IMAGE PAIRS. THE AREA MATCHING AND POSE ESTIMATION PERFORMANCE ARE REPORTED. THE NUMBERS OF AREA MATCHES (NUM) ARE ALSO REPORTED.

SOA	SIA	GP	GR	GMC	AOR ↑	AMP ↑	Num	AUC@5 °↑	AUC@10 °↑	AUC@20 °↑
✓					79.39	78.88	2.74	32.96	43.77	53.80
✓	✓				74.64	69.42	2.11	31.72	40.66	46.89
✓	✓				77.41	74.95	4.53	34.02	48.26	52.94
✓	✓	✓			79.03	76.30	5.57	39.54	52.97	64.54
✓	✓	✓	✓		79.01	78.00	3.73	49.24	62.01	73.32
✓	✓	✓	✓		79.18	78.27	4.01	49.73	62.58	73.17
✓	✓	✓	✓	✓	79.18	78.27	4.01	50.50	63.38	74.75

TABLE XI

TIME CONSUMPTION COMPARISON. THE EXPERIMENT IS CONDUCTED ON SCANNET WITH FD@10. THE TIME CONSUMPTION OF EACH COMPONENT OF OUR METHOD WITH SPECIFIC INPUT SIZE IS REPORTED. DIFFERENT TIME CONSUMPTION COMES FROM DIFFERENT BASELINES COUPLED WITH OUR METHOD ARE INVESTIGATED AS WELL. THE TIME OF BASELINES ARE ALSO REPORTED.

Time/s	Input Size					
	640×480		256×256			640×480
PM	SAM	GP	GR	GMC	SGAM	PM
Aspan		0.042	0.20	0.021	0.88	0.19
QuadT	0.62	0.040	0.17	0.023	0.85	0.18
LoFTR		0.041	0.19	0.018	0.86	0.18
COTR		2.54	23.85	2.13	29.14	56.04

are reported in Tab. X. It can be seen that both area matching and pose estimation accuracy improve as the completeness of our method increases. This finding confirms the effectiveness of all the components within our SGAM approach.

J. Discussion on the Computational Complexity

In this section, we discuss in detail the theoretical computational complexity of each component of our proposed approach, including SAM, GP and GR. Moreover, we conduct an experiment to count the average running time per image pair of each component of our method in practice. We collect 1500 sets of image pairs from ScanNet with FD@10 for this experiment. Four baseline point matchers are combined for time comparison. The results are reported in Tab. XI. This experiment is run on a Intel Xeon Silver 4314 CPU and a GeForce RTX 4090 GPU.

1) *Computational Complexity of SAM.* SAM mainly includes area detection and description for two semantic areas (SOA and SIA). For SOA, the size of the algorithm is related to the number of semantic categories in the image pair (N_{sem}). Thus the computational complexity for this part is $O(N_{sem})$. The SIA part involves a sliding window algorithm on image. Its computational complexity is $O((W_I - W_w) * (H_I - H_w)/s^2)$, where W_I, H_I are the Width and Height of the Image, W_w, H_w are Width and Height of window and s is the sliding step. As the window size is large (please refer to Sec. IV-A2), the time consumption of this part is acceptable. 2) *Computational Complexity of GP.* Given H doubtful areas in I_0 and R in I_1 , the GP can determine area matches through point matching within areas. Relying on correspondences, however, leads to multiple times point matching for all area

match possibilities ($H \times R$ times) in the single image pair. At the same time, the calculation of $P(As_i)$ in Eq. 9 also need to be performed $L = \frac{H!}{(H-R)!}$ times. Thus, for $P(As_i)$ calculation, its computational complexity varies from $O(N)$ (when $R = 1$) to $O(N!)$ (when $R = H - 1$), depending on the area number. However, as we only perform this prediction when semantic ambiguity occurs, the practical time cost is acceptable, as shown in Tab. XI.

3) *Computational Complexity of GR.* In GR, point matching inside area matches are performed to compute geometry consistency. This inside-area matching is the key of our A2PM framework, which is equivalent to decomposing a large matching problem (the full-image matching) into multiple smaller matching problems. The computational complexity of widely-used vanilla Transformer in SOTA matching method [37] is $O(N^2)$, where N is the input size. Thus, this decomposing of matching in A2PM is more efficient than direct matching, when the area size is smaller enough than the original image size. Specifically, suppose the image size is $W_I \times H_I$, area size is $W_a \times H_a$ and area match number is N_a . Then the computational complexity of original point matcher is $O((W_I \times H_I)^2)$, while the computational complexity of A2PM is $O(N_a \times (W_a \times H_a)^2)$. Thus, our A2PM is more effective than the original point matcher, when $(W_I \times H_I)^2 / (W_a \times H_a)^2 \geq N_a$. Some recent methods use linear Transformer whose computational complexity is $O(N)$. In this case, our A2PM is more effective than the original point matcher, when $(W_I \times H_I) / (W_a \times H_a) \geq N_a$. The specific time consumption of our method is reported in Tab. XI for ScanNet. The area size is 256×256 and the image size is 640×480 in the experiments. It can be seen that our GR costs similar time as the original PM, when linear Transformer is used (ASpan, QuadT and LoFTR). However, the overall time consumption of our SGAM is more than direct PM. This is primarily attributed to the slower speed of SAM, as we have not yet optimized it for efficiency in engineering. On the other hand, our method is faster than direct PM with vanilla Transformer (COTR), because of its second-order computational complexity.

K. Advantages and Limitations

As semantic possesses consistency against various matching noises, e.g. illumination, viewpoint and scale changes between images, our SGAM is able to find accurate area matches in challenging scenes. Then, the precision of inside-area point matching is significantly boosted, due to noise removal and higher resolution of these areas, which is the main advantage of our method. We also provide qualitative comparison results for five hard scenarios in Fig. 11 to demonstrate the superiority of SGAM. However, heavy reliance on semantics also results in limitations of SGAM. First, the semantic segmentation accuracy impacts the performance of our method. Especially for area matching, our SAM and GP exhibits non-negligible decreases in precision (Tab. VII and Tab. VIII). This is because the area detection and description in SAM both assume accurate semantic input. Thus the under-splitting, over-splitting, and multiple semantics in inferior semantic segmentation leads to reduced performance of SAM and large

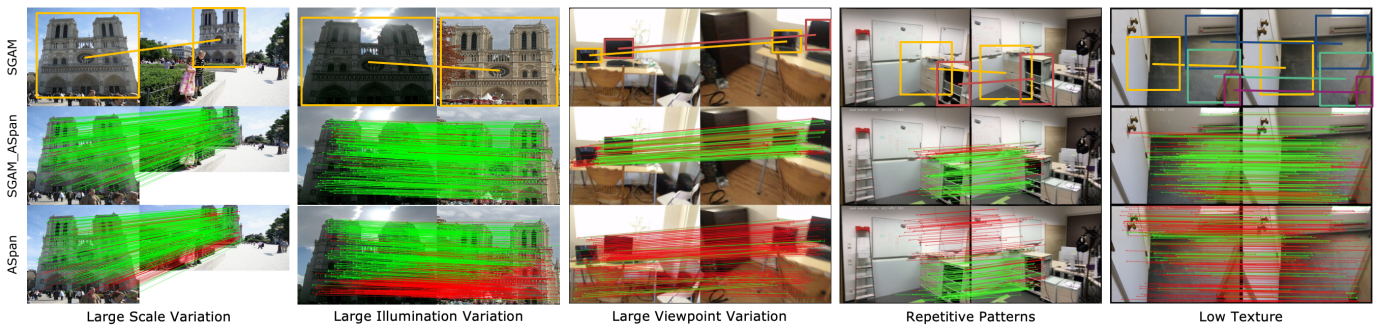


Fig. 11. **Qualitative Comparison on challenging scenes.** The visual comparison between our method and ASpan in challenging scenes. The **wrong** and **correct** matches under the same threshold are labeled respectively.

doubtful area numbers for GP. However, it is noteworthy that SGAM is still able to improve the point matching and pose estimation performance with SEEM-L/T in our experiments. This highlights the fact that the advantages of SGAM are still significant in the presence of less accurate semantic inputs and implies the potential of our A2PM framework. The second limitation of SGAM is related to the spatial granularity of semantic categories. For example, when a single semantic entity dominates the image, it is difficult for SAM to find areas with clustered features. Hence the effectiveness of SGAM is restricted in some scenes, such as YFCC100M. However, in such scenes, the A2PM framework still benefits feature matching, but the area matches need to be established by other approaches, like overlap estimation [14], [53]. In our future work, we will focus on area matching without semantic prior, which may work well in more general application scenes.

VI. CONCLUSION

From a unified searching perspective, this paper proposes semantic area matches, which are matched areas with prominent semantic, to serve as the proper search space for precise feature matching. This search space effectively reduces the matching difficulty and provides point matchers with high resolution input, ultimately improving the matching performance. We propose the A2PM framework as the corresponding search strategy for this search space, which hierarchically divides the feature matching into two search phases: establishing semantic area matches on the entire image and finding point matches from these area matches. To implement the A2PM framework, we propose SGAM comprises SAM and GAM, to leverage both semantic information and geometry constraint of images. The SAM performs rough area matching based on semantic cues. On the other hand, the GAM, integrated with an off-the-shelf point matcher, achieves accurate area and point matches based on the geometry consistency. Extensive experiments demonstrate the effectiveness of our approaches, which significantly outperform other SOTA methods in both image matching task and down-stream pose estimation task.

REFERENCES

- [1] C. Cadena, L. Carlone, H. Carrillo, Y. Latif, D. Scaramuzza, J. Neira, I. Reid, and J. J. Leonard, "Past, present, and future of simultaneous localization and mapping: Toward the robust-perception age," *IEEE Transactions on Robotics*, vol. 32, no. 6, pp. 1309–1332, 2016.
- [2] J. L. Schonberger and J.-M. Frahm, "Structure-from-motion revisited," in *Proceedings of the IEEE conference on computer vision and pattern recognition*, 2016, pp. 4104–4113.
- [3] P. Truong, S. Apostolopoulos, A. Mosinska, S. Stucky, C. Ciller, and S. D. Zanet, "Glampoints: Greedily learned accurate match points," in *Proceedings of the IEEE/CVF International Conference on Computer Vision*, 2019, pp. 10732–10741.
- [4] D. G. Lowe, "Distinctive image features from scale-invariant keypoints," *International journal of computer vision*, vol. 60, no. 2, pp. 91–110, 2004.
- [5] D. DeTone, T. Malisiewicz, and A. Rabinovich, "Superpoint: Self-supervised interest point detection and description," *Proceedings of the IEEE conference on computer vision and pattern recognition workshops*, pp. 224–236, 2018.
- [6] Z. Shen, J. Sun, Y. Wang, X. He, H. Bao, and X. Zhou, "Semi-dense feature matching with transformers and its applications in multiple-view geometry," *IEEE Transactions on Pattern Analysis and Machine Intelligence*, pp. 1–12, 2022.
- [7] H. Chen, Z. Luo, L. Zhou, Y. Tian, M. Zhen, T. Fang, D. McKinnon, Y. Tsin, and L. Quan, "Aspanformer: Detector-free image matching with adaptive span transformer," in *Computer Vision—ECCV 2022: 17th European Conference, Tel Aviv, Israel, October 23–27, 2022, Proceedings, Part XXXII*. Springer, 2022, pp. 20–36.
- [8] X. Zhao, X. Wu, J. Miao, W. Chen, P. C. Chen, and Z. Li, "Alike: Accurate and lightweight keypoint detection and descriptor extraction," *IEEE Transactions on Multimedia*, 2022.
- [9] Z. Luo, L. Zhou, X. Bai, H. Chen, J. Zhang, Y. Yao, S. Li, T. Fang, and L. Quan, "Aslfeat: Learning local features of accurate shape and localization," *Computer Vision and Pattern Recognition (CVPR)*, 2020.
- [10] J. Sun, Z. Shen, Y. Wang, H. Bao, and X. Zhou, "LoFTR: Detector-free local feature matching with transformers," *CVPR*, 2021.
- [11] S. Tang, J. Zhang, S. Zhu, and P. Tan, "Quadtree attention for vision transformers," *ICLR*, 2022.
- [12] J. Yu, J. Chang, J. He, T. Zhang, J. Yu, and W. Feng, "ASTR: Adaptive spot-guided transformer for consistent local feature matching," *CVPR*, 2023.
- [13] D. Huang, Y. L. Ying Chen, S. X. Jianlin Liu, F. T. Wenlong Wu, Yikang Ding, and C. Wang, "Adaptive assignment for geometry aware local feature matching," *CVPR*, 2023.
- [14] H. Song, Y. Kashiwaba, S. Wu, and C. Wang, "Efficient and accurate co-visible region localization with matching key-points crop (mkpc): A two-stage pipeline for enhancing image matching performance," *arXiv preprint arXiv:2303.13794*, 2023.
- [15] Y. L. Junjie Ni, H. L. Zhaoyang Huang, Z. C. Hujun Bao, and G. Zhang, "Pats: Patch area transportation with subdivision for local feature matching," in *The IEEE/CVF Computer Vision and Pattern Recognition Conference (CVPR)*, 2023.
- [16] X. Zou, J. Yang, H. Zhang, F. Li, L. Li, J. Gao, and Y. J. Lee, "Segment everything everywhere all at once," *arXiv preprint arXiv:2304.06718*, 2023.
- [17] J. L. Schönberger, M. Pollefeys, A. Geiger, and T. Sattler, "Semantic visual localization," in *Proceedings of the IEEE conference on computer vision and pattern recognition*, 2018, pp. 6896–6906.
- [18] Y. Bao, Z. Yang, Y. Pan, and R. Huan, "Semantic-direct visual odometry," *IEEE Robotics and Automation Letters*, vol. 7, no. 3, pp. 6718–6725, 2022.
- [19] B. Fan, J. Zhou, W. Feng, H. Pu, Y. Yang, Q. Kong, F. Wu, and H. Liu, "Learning semantic-aware local features for long term visual localization," *IEEE Transactions on Image Processing*, vol. 31, pp. 4842–4855, 2022.
- [20] E. Rublee, V. Rabaud, K. Konolige, and G. Bradski, "Orb: An efficient alternative to sift or surf," *2011 International conference on computer vision*, pp. 2564–2571, 2011.
- [21] J. Revaud, C. De Souza, M. Humenberger, and P. Weinzaepfel, "R2d2: Reliable and repeatable detector and descriptor," *Advances in neural information processing systems*, vol. 32, 2019.

- [22] M. Tyszkiewicz, P. Fua, and E. Trulls, “Disk: Learning local features with policy gradient,” *Advances in Neural Information Processing Systems*, vol. 33, pp. 14 254–14 265, 2020.
- [23] M. Dusmanu, I. Rocco, T. Pajdla, M. Pollefeys, J. Sivic, A. Torii, and T. Sattler, “D2-net: A trainable cnn for joint description and detection of local features,” *Proceedings of the IEEE/CVF conference on computer vision and pattern recognition*, pp. 8092–8101, 2019.
- [24] A. Barroso-Laguna, E. Riba, D. Ponsa, and K. Mikolajczyk, “Key. net: Keypoint detection by handcrafted and learned cnn filters,” *Proceedings of the IEEE/CVF International Conference on Computer Vision*, pp. 5836–5844, 2019.
- [25] G. Bökman and F. Kahl, “A case for using rotation invariant features in state of the art feature matchers,” *Proceedings of the IEEE/CVF Conference on Computer Vision and Pattern Recognition*, pp. 5110–5119, 2022.
- [26] J. Lee, B. Kim, and M. Cho, “Self-supervised equivariant learning for oriented keypoint detection,” *Proceedings of the IEEE/CVF Conference on Computer Vision and Pattern Recognition (CVPR)*, June 2022.
- [27] T. Ng, H. J. Kim, V. T. Lee, D. DeTone, T.-Y. Yang, T. Shen, E. Ilg, V. Balntas, K. Mikolajczyk, and C. Sweeney, “Ninjadesc: Content-concealing visual descriptors via adversarial learning,” *Proceedings of the IEEE/CVF Conference on Computer Vision and Pattern Recognition*, pp. 12 797–12 807, 2022.
- [28] J. Revaud, V. Leroy, P. Weinzaepfel, and B. Chidlovskii, “Pump: Pyramidal and uniqueness matching priors for unsupervised learning of local descriptors,” *Proceedings of the IEEE/CVF Conference on Computer Vision and Pattern Recognition*, pp. 3926–3936, 2022.
- [29] K. Li, L. Wang, L. Liu, Q. Ran, K. Xu, and Y. Guo, “Decoupling makes weakly supervised local feature better,” *Proceedings of the IEEE/CVF Conference on Computer Vision and Pattern Recognition*, pp. 15 838–15 848, 2022.
- [30] P.-E. Sarlin, D. DeTone, T. Malisiewicz, and A. Rabinovich, “Superglue: Learning feature matching with graph neural networks,” *Proceedings of the IEEE/CVF Conference on Computer Vision and Pattern Recognition (CVPR)*, June 2020.
- [31] Z. Zhong, G. Xiao, L. Zheng, Y. Lu, and J. Ma, “T-net: Effective permutation-equivariant network for two-view correspondence learning,” in *Proceedings of the IEEE/CVF International Conference on Computer Vision (ICCV)*, October 2021, pp. 1950–1959.
- [32] J. Zhang, D. Sun, Z. Luo, A. Yao, L. Zhou, T. Shen, Y. Chen, L. Quan, and H. Liao, “Learning two-view correspondences and geometry using order-aware network,” in *Proceedings of the IEEE/CVF International Conference on Computer Vision (ICCV)*, October 2019.
- [33] Y. Xia and J. Ma, “Locality-guided global-preserving optimization for robust feature matching,” *IEEE Transactions on Image Processing*, vol. 31, pp. 5093–5108, 2022.
- [34] L. Zheng, G. Xiao, Z. Shi, S. Wang, and J. Ma, “Msa-net: Establishing reliable correspondences by multiscale attention network,” *IEEE Transactions on Image Processing*, vol. 31, pp. 4598–4608, 2022.
- [35] X. Liu, G. Xiao, R. Chen, and J. Ma, “Pgfnet: Preference-guided filtering network for two-view correspondence learning,” *IEEE Transactions on Image Processing*, vol. 32, pp. 1367–1378, 2023.
- [36] I. Rocco, M. Cimpoi, R. Arandjelović, A. Torii, T. Pajdla, and J. Sivic, “Neighbourhood consensus networks,” *Advances in neural information processing systems*, vol. 31, 2018.
- [37] W. Jiang, E. Trulls, J. Hosang, A. Tagliasacchi, and K. M. Yi, “Cotr: Correspondence transformer for matching across images,” in *Proceedings of the IEEE/CVF International Conference on Computer Vision*, 2021, pp. 6207–6217.
- [38] I. Rocco, R. Arandjelović, and J. Sivic, “Efficient neighbourhood consensus networks via submanifold sparse convolutions,” *European conference on computer vision*, pp. 605–621, 2020.
- [39] L. Xinghui, H. Kai, L. Shuda, and V. P. Adrian, “Dual-resolution correspondence networks,” *NIPS*, pp. 17 346–17 357, 2020.
- [40] J. Edstedt, I. Athanasiadis, M. Wadenbäck, and M. Felsberg, “DKM: Dense kernelized feature matching for geometry estimation,” *CVPR*, 2023.
- [41] A. Vaswani, N. Shazeer, N. Parmar, J. Uszkoreit, L. Jones, A. N. Gomez, Ł. Kaiser, and I. Polosukhin, “Attention is all you need,” *Advances in neural information processing systems*, vol. 30, 2017.
- [42] R. Hartley and A. Zisserman, “Multiple view geometry in computer vision,” *Cambridge university press*, 2003.
- [43] A. Dai, A. X. Chang, M. Savva, M. Halber, T. Funkhouser, and M. Nießner, “ScanNet: Richly-annotated 3d reconstructions of indoor scenes,” *Proc. Computer Vision and Pattern Recognition (CVPR)*, *IEEE*, 2017.
- [44] A. Chang, A. Dai, T. Funkhouser, M. Halber, M. Niessner, M. Savva, S. Song, A. Zeng, and Y. Zhang, “Matterport3d: Learning from rgb-d data in indoor environments,” *International Conference on 3D Vision (3DV)*, 2017.
- [45] Y. Liao, J. Xie, and A. Geiger, “Kitti-360: A novel dataset and benchmarks for urban scene understanding in 2d and 3d,” *IEEE Transactions on Pattern Analysis and Machine Intelligence*, 2022.
- [46] B. Thomee, D. A. Shamma, G. Friedland, B. Elizalde, K. Ni, D. Poland, D. Borth, and L.-J. Li, “YFCC100M: The new data in multimedia research,” *Communications of the ACM*, vol. 59, no. 2, pp. 64–73, 2016.
- [47] J. Yang, C. Li, X. Dai, and J. Gao, “Focal modulation networks,” *Advances in Neural Information Processing Systems (NeurIPS)*, 2022.
- [48] T.-Y. Lin, M. Maire, S. Belongie, J. Hays, P. Perona, D. Ramanan, P. Dollár, and C. L. Zitnick, “Microsoft coco: Common objects in context,” in *Computer Vision—ECCV 2014: 13th European Conference, Zurich, Switzerland, September 6–12, 2014, Proceedings, Part V 13*. Springer, 2014, pp. 740–755.
- [49] H. Chen, Z. Luo, J. Zhang, L. Zhou, X. Bai, Z. Hu, C.-L. Tai, and L. Quan, “Learning to match features with seeded graph matching network,” in *Proceedings of the IEEE/CVF International Conference on Computer Vision*, 2021, pp. 6301–6310.
- [50] X. Li, K. Han, S. Li, and V. Prisacariu, “Dual-resolution correspondence networks,” *Advances in Neural Information Processing Systems*, vol. 33, pp. 17 346–17 357, 2020.
- [51] Q. Wang, J. Zhang, K. Yang, K. Peng, and R. Stiefelhagen, “Match-former: Interleaving attention in transformers for feature matching,” in *Proceedings of the Asian Conference on Computer Vision*, 2022, pp. 2746–2762.
- [52] X. Lu, Y. Yan, T. Wei, and S. Du, “Scene-aware feature matching,” in *Proceedings of the IEEE/CVF International Conference on Computer Vision*, 2023, pp. 3704–3713.
- [53] Y. Chen, D. Huang, S. Xu, J. Liu, and Y. Liu, “Guide local feature matching by overlap estimation,” in *Proceedings of the AAAI Conference on Artificial Intelligence*, vol. 36, no. 1, 2022, pp. 365–373.